Inferring biological processes with intrinsic noise from cross-sectional data

Suryanarayana Maddu,[1, *] Victor Chardès,[1, *] and Michael. J. Shelley[1, 2]

[1]*Center for Computational Biology, Flatiron Institute, New York, NY, USA, 10010*
[2]*Courant Institute of Mathematical Sciences, New York University, New York, NY, USA, 10012*

Inferring dynamical models from data continues to be a significant challenge in computational biology, especially given the stochastic nature of many biological processes. We explore a common scenario in omics, where statistically independent cross-sectional samples are available at a few time points, and the goal is to infer the underlying diffusion process that generated the data. Existing inference approaches often simplify or ignore noise intrinsic to the system, compromising accuracy for the sake of optimization ease. We circumvent this compromise by inferring the phase-space probability flow that shares the same time-dependent marginal distributions as the underlying stochastic process. Our approach, probability flow inference (PFI), disentangles force from intrinsic stochasticity while retaining the algorithmic ease of ODE inference. Analytically, we prove that for Ornstein-Uhlenbeck processes the regularized PFI formalism yields a unique solution in the limit of well-sampled distributions. In practical applications, we show that PFI enables accurate parameter and force estimation in high-dimensional stochastic reaction networks, and that it allows inference of cell differentiation dynamics with molecular noise, outperforming state-of-the-art approaches.

I. INTRODUCTION

From gene expression [1, 2], collective motion in animal groups [3, 4], to growth in ecological communities [5], the behavior of biological processes is driven by a dynamic interplay between deterministic mechanisms and intrinsic noise. In these systems, stochasticity plays a pivotal role, often leading to outcomes that diverge significantly from those predicted by deterministic frameworks [4, 6, 7]. To elucidate the respective roles of deterministic forces and intrinsic noise, many inference approaches exploit time-correlations in high-resolution stochastic trajectories [8, 9]. Comparatively, inferring biological processes at a single-cell level presents a unique challenge: due to the destructive nature of the single-cell omics measurements, we can only observe statistically independent cross-sectional samples from the latent stochastic process [10, 11]. This limitation imposes fundamental constraints on the identifiable dynamics and makes it difficult to disentangle deterministic forces from intrinsic noise [12, 13].

In this study, we investigate this issue for systems that can be modeled as diffusion processes [8], for which the continuous-time evolution of the degrees of freedom $\mathbf{x} \in \mathbb{R}^d$ follows a stochastic differential equation (SDE) [14]. Under the assumption that there are no exogenous factor or unobserved variable driving the evolution of the system, we consider autonomous Itô processes of the form

$$d\mathbf{x} = \mathbf{f}(\mathbf{x})dt + \sqrt{2}\mathbf{G}(\mathbf{x})d\mathbf{W}, \qquad (1)$$

where $\mathbf{W}$ is a standard d-dimensional Wiener process, $\mathbf{f} : \mathbb{R}^d \rightarrow \mathbb{R}^d$ is a deterministic force and $\mathbf{G} : \mathbb{R}^d \rightarrow \mathbb{R}^{d \times d}$ the intrinsic noise model. Many molecular processes in cells have been shown to follow negative binomial statistics [15, 16], revealing a strong correlation between

the amplitude of regulation and intrinsic noise. As a result, a biologically plausible intrinsic noise model $\mathbf{G}(\mathbf{x})$ can be force and state-dependent.

The formulation via Eq. (1) in terms of stochastic trajectories $\{\mathbf{x}(t), t \geq 0\}$ is equivalent to a formulation in terms of the transition probability $p(\mathbf{x}, t|\mathbf{y}, s)$, which describes the probability to reach the state $\mathbf{x}$ at time t, having started in $\mathbf{y}$ at time s [14]. Its evolution obeys the Kolmogorov forward equation,

$$\partial_t p(\mathbf{x}, t|\mathbf{y}, s) = - \nabla \cdot \Bigg[\mathbf{f}(\mathbf{x})p(\mathbf{x}, t|\mathbf{y}, s)$$
$$- \nabla \cdot (\mathbf{D}(\mathbf{x})p(\mathbf{x}, t|\mathbf{y}, s)) \Bigg], \qquad (2)$$

for all $\mathbf{x}, \mathbf{y} \in \mathbb{R}^d$, $t, s \geq 0$, with $\mathbf{D} = \mathbf{G}\mathbf{G}^T \in \mathbb{S}_+^d$, and divergences applied row-wise on tensor-valued functions. When time-resolved trajectories are available, both the force field and the diffusion can be inferred simultaneously by fitting either of these equations to the data [8]. To simplify computations, most approaches rely on discretizing Eq. (1) rather than fitting transition probabilities with Eq. (2), with successful applications in fields such as soft matter and finance [8, 17–19].

However, with single-cell omics data, the lack of trajectory information makes it impossible to reconstruct the transition probabilities $p(\mathbf{x}, t|\mathbf{y}, s)$. Within this setting, it is more appropriate to model the evolution of marginal distributions over time with the Fokker-Planck equation

$$\partial_t p_t(\mathbf{x}) = -\nabla \cdot \left[\mathbf{f}(\mathbf{x})p_t(\mathbf{x}) - \nabla \cdot (\mathbf{D}(\mathbf{x})p_t(\mathbf{x}))\right], \quad (3)$$

which is obtained by marginalizing Eq. (2) over an initial conditions $p_0(\mathbf{y})$. The inverse problem now reduces to learning how the probability mass is moved between empirical distributions at successive time points rather than how one trajectory evolves. Unlike trajectory-based methods, it is no longer possible to infer both the force and noise models simultaneously, requiring a prior on one to infer the other.

---
* These authors contributed equally to this work

Approaches based on optimal transport have been used to tackle this question, first in static settings by learning pairwise couplings between successive empirical distributions, and subsequently in dynamical settings by learning a time-continuous model connecting distributions at all times. While static methods cannot model time-continuous and non-linear dynamics [11, 20–23], their dynamical counterparts lift these constraints, but all methods remain limited to additive priors on the noise model [24–27]. Other approaches that integrate trajectory data with mechanistic differential equation models also use deterministic frameworks [28] or assume additive noise [29, 30]. Even popular methods that infer cell-fate directionality from messenger RNA splicing and spatial transcriptomics data also adopt additive noise models for parameter estimation [31]. However, force and state-dependent noise models not only better capture biological variability, but they also have the capacity to shift, create, or eliminate fixed points in the energy landscape, which is of paramount importance to model processes like cell differentiation [1, 2, 6]. This underscores the need for inference methods that accommodate molecular noise while retaining algorithmic simplicity.

We introduce Probability Flow Inference (PFI), a method that separates the force field from any intrinsic noise model while retaining the computational efficiency of ODE optimization. First, by analytically solving the PFI approach for Ornstein-Uhlenbeck (OU) processes, we prove that the inverse problem admits a unique solution when the force field is regularized, and that without regularization it can lead to infinitely many solutions. By focusing on a subclass of isotropic OU processes, we show that all non-conservative force contributions can be recovered in the limit of vanishingly small regularization. We contrast this observation by demonstrating the existence of a bias-variance trade-off coming from finite sampling of the cross-sectional data, thereby advocating for a non-zero regularization. Finally, with the same analytical solution we show that a good prior on intrinsic noise is necessary to accurately infer the underlying force field.

Building on these theoretical insights, we apply the PFI approach to stochastic reaction networks, widely used to model cellular processes. We show that PFI reliably infers the continuous diffusion approximation of these discrete-state stochastic processes, with a particular focus on estimating rate parameters and inferring gene regulatory networks. In agreement with our theoretical results for the OU processes, we underscore the importance of an informed biophysical prior on the noise model to achieve accurate force inference. Finally, using a curated hematopoietic stem cell model, we demonstrate that PFI outperforms state-of-the-art generative models in inferring cell differentiation dynamics and predicting in-silico gene knockdown perturbations.

METHODOLOGY

Problem statement

We assume that the data is given as $K + 1$ statistically independent cross-sectional snapshots, each composed of n samples, taken from the true process at successive times $t_0 = 0 < ... < t_i < ... < t_K = T$, with uniform spacing Δt. We further assume that the n i.i.d samples $\{\mathbf{x}_{k,t_i}, 1 \leq k \leq n\}$ are measured at each time t_i from the true marginals, giving access to an empirical estimator of p_{t_i},

$$p_{t_i}(\mathbf{x}) \approx \frac{1}{n} \sum_{k=1}^{n} \delta(\mathbf{x} - \mathbf{x}_{k,t_i}).$$

The objective is to infer the force field $\mathbf{f}(\mathbf{x})$ associated with a latent stochastic process interpolating the observed marginals. Since it is not possible to simultaneously infer both the force field and diffusion from statistically independent cross-sectional samples, we impose strong priors on the noise model. For example, in the case of molecular noise arising from chemical reactions, the diffusion tensor $\mathbf{D}(\mathbf{x})$ is force and state dependent and follows a known functional form [32]. We leverage such intrinsic noise priors to accurately infer the force fields and reconstruct the underlying stochastic dynamics.

Probability flow inference (PFI)

A common approach to inferring the force field $\mathbf{f}(\mathbf{x})$ is to fit the SDE by minimizing a distance metric between the observed empirical marginals and the generated samples, in a *predict* and *correct* manner [33, 34]. However, this optimization is both memory- and compute-intensive, and is limited to additive or diagonal noise models [34]. As previously noted, we can improve on this by observing that the SDE formulation Eq. (1) contains redundant information for modeling the evolution of marginals, and that Eq. (3) is sufficient.

Hence, instead of fitting the SDE, we use the probability flow ODE, which reproduces the same marginal distributions $p_t(\mathbf{x})$ as the underlying SDE [35, 36]. The probability flow ODE reads

$$\frac{d\mathbf{x}}{dt} = \mathbf{f}(\mathbf{x}) - \nabla \cdot \mathbf{D}(\mathbf{x}) - \mathbf{D}(\mathbf{x})\nabla \log p_t(\mathbf{x}), \qquad (4)$$

and the term $\nabla \log p_t(\mathbf{x})$, or the gradient of the log-probability of the marginals, is known as the score [37]. The PFI approach consists of two steps: (i) estimating the score function, and (ii) fitting the probability flow ODE Eq. (4) to the observed marginals. This ODE approach allows for the use of accurate forward solvers [38] and constant-memory gradient computations [39] to fit the force field. More broadly, and relevant to PFI, reverse-mode automatic differentiation tools now allow the fitting
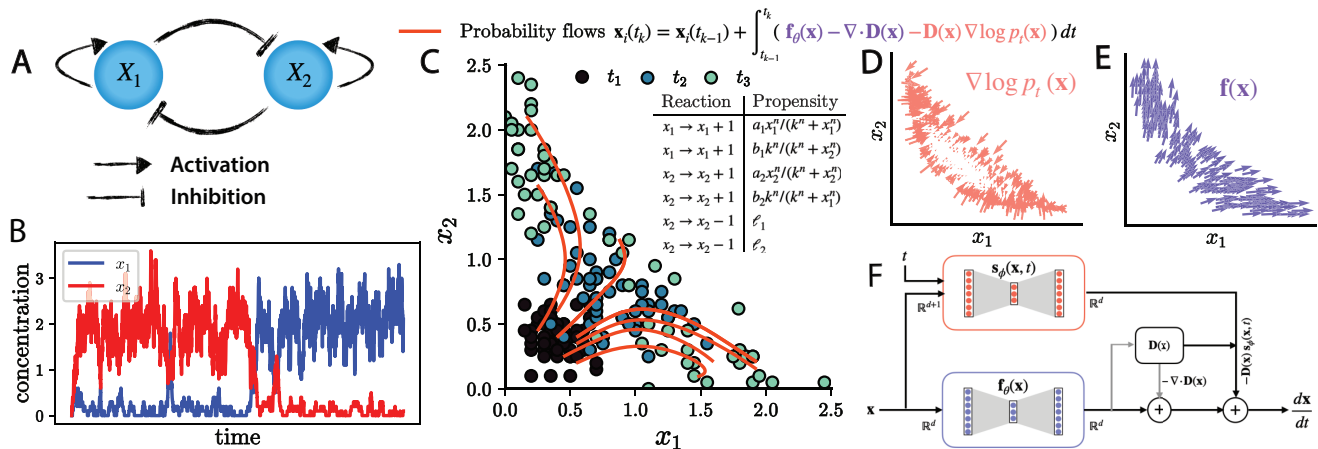
FIG. 1. **Probability flow inference**. **A.** Dynamics of the canonical fate decision regulatory circuit of two mutually opposing transcription factors (x_1, x_2) that positively self-regulate themselves. **B.** Time series generated from direct stochastic simulation (Gillespie algorithm) of the toggle-switch model showing the concentration levels of x_1 (blue) and x_2 (red), illustrating their dynamics over time. The Gillespie simulation was run with parameters $a_1 = a_2 = b_1 = b_2 = k = 1.0$, and $n = 4$. The degradation rates are $\ell_1 = \ell_2 = 1$. **C.** Cross-sectional snapshots generated from the discrete Gillespie simulations at time points $\{t_1, t_2, t_3\}$ represent the marginals' evolution through the stochastic process. Characteristics lines (in red) show the probability flows deforming the initial state t_1 to a future state t_3 in the state space, illustrating the dynamic transition of the systems state. The inset describes the reactions and associated propensities of the two-gene fate decision circuit shown in **A**. Score (**D**) and force (**E**) approximation at time t_1. **F.** Network architecture of our probability flow inference (PFI) approach. Both the autonomous force field $\mathbf{f}_\theta(\mathbf{x}) : \mathbf{R}^d \to \mathbb{R}^d$ and the time-dependent score model $\mathbf{s}_\phi(\mathbf{x}, t) : \mathbb{R}^{d+1} \to \mathbb{R}^d$ are parameterized using feedforward networks, with parameters θ and ϕ, respectively.

of ODEs with millions of parameters to data [39], enabling more flexible approaches to density estimation and time series modeling [40, 41].

We now outline the two steps of the PFI approach:

Score estimation: The first step of the PFI approach requires estimating the time-dependent score function from empirical samples at various time points. To efficiently solve this task we leverage recent advancements in generative modeling that allow fast and accurate score estimation in high-dimensions [42, 43]. Specifically, we use sliced score matching (Materials and Methods) to train a score network $\mathbf{s}_\phi(\mathbf{x}, t)$ that approximates $\nabla \log p_t(\mathbf{x})$.

Force inference: Once an accurate score model is available, we seek to fit the force via Eq. (4) to the observed marginals. In many cases, it is impossible to uniquely identify a force field $\mathbf{f}(\mathbf{x})$ satisfying Eq. (3) and matching the empirical marginals. To see this, consider two force fields $\mathbf{f}(\mathbf{x})$ and $\mathbf{g}(\mathbf{x}) = \mathbf{f}(\mathbf{x}) + \mathbf{h}(\mathbf{x})$. Both yield the same marginal distribution $p_t(\mathbf{x})$ as $\mathbf{f}(\mathbf{x})$ if $\mathbf{h}(\mathbf{x})$ satisfies

$$\nabla \cdot \mathbf{h}(\mathbf{x}) + \mathbf{h}(\mathbf{x}) \cdot \nabla \log p_t(\mathbf{x}) = 0, \ \forall \, t \geq 0, \quad (5)$$

at every position $\mathbf{x}$. If the data is initialized such that $\nabla \log p_t(\mathbf{x}) \propto \mathbf{x}$, which is the case for an isotropic OU process initialized with an isotropic Gaussian initial condition, a solution of Eq. (5) is given by $\hat{\mathbf{h}}(\mathbf{x}) = \mathbf{K}\mathbf{x}$, for any skew-symmetric matrix $\mathbf{K}$. This lack of uniqueness, referred to as the identifiability issue, has been of long standing concern in the analysis of single-cell RNA-seq data [6, 13, 33].

In statistical physics, the component of the force field

$\mathbf{f}(\mathbf{x})$ that satisfies equation Eq. (5) in the limit $t \to \infty$ is referred to as the non-conservative force as it induces non-zero phase-space probability currents at steady-state [14]. The knowledge of such non-conservative forces is instrumental to accurately predict cell differentiation and cell reprogramming pathways [44, 45]. The remaining part of the force is termed the conservative force and it alone balances the effect of diffusion. While the non-conservative force cannot be uniquely identified from the temporal evolution of the marginals (when Eq. (5) admits non-trivial solutions), the conservative force can always be inferred, even at a steady state. In summary, the identifiability issue is equivalent to the problem of identifying contributions to the force driving irreversible cycles in state-space.

To circumvent this ill-posedness, we choose to introduce an ℓ_2-regularization on the Jacobian matrix of the inferred force field to the loss function which reads

$$\mathcal{L}_{\Delta t, K} = \sum_{i=1}^{K} \left[\mathcal{W}_2^2(\hat{p}_{t_i}(\mathbf{x}), p_{t_i}(\mathbf{x})) \right.$$
$$\left. + \lambda \Delta t \int \int_{t_{i-1}}^{t_i} \|\nabla \hat{\mathbf{f}}(\mathbf{x})\|_F^2 p_{t_i}(\mathbf{x}) d\mathbf{x} dt \right]. \quad (6)$$

Here $\lambda \geq 0$ is a tunable parameter that controls the strength of regularization, and $\mathcal{W}_2$ is the Wasserstein distance between the empirically observed distribution $p_{t_i}(\mathbf{x})$ and the predicted distribution $\hat{p}_{t_i}(\mathbf{x})$. Though the above regularization penalizes the curvature of the

force field, any other regularization minimizing the kinetic energy is also appropriate [24].

Computing the exact Wasserstein distance $\mathcal{W}_2$ requires $\mathcal{O}(n^3 \log n)$ operations, and it estimation in d dimensions has a sample complexity of $\mathcal{O}(n^{-1/d})$. Its entropy-regularized version, known as the Sinkhorn divergence, reduces the computational cost to $\mathcal{O}(n^2)$ with a dimension-independent sample complexity $\mathcal{O}(n^{-1/2})$ for large entropic regularization [46, 47]. For computational reasons the choice of distance is problem-specific: for uni-modal marginal distributions we approximate the empirical Wasserstein distance with its Gaussian estimator [48], and for complex multimodal distributions we use the Sinkhorn divergences. Before stepping into numerical examples, in the next section we study analytically the identifiability issue for OU processes.

Analytical case study: Ornstein-Uhlenbeck process

Linear models are a very popular choice for gene regulatory network inference [49], and reconstructing cellular dynamics based on RNA velocity [50, 51]. Despite their frequent use for such inference tasks, the challenges related to the identifiability issue, the role of regularization, and various sources of error are never addressed. In this section we tackle this issue in a continuous-time limit, $\Delta t \to 0$, with which we establish a uniqueness result for the inferred process in the presence of regularization. For this purpose, we assume that the underlying latent process to be inferred is a d-dimensional OU process with an interaction matrix $\boldsymbol{\Omega}$. That is,

$$d\mathbf{x} = \boldsymbol{\Omega}\mathbf{x}dt + \sqrt{2\mathbf{D}}d\mathbf{W}, \text{ with } \mathbf{x}_0 \sim p_0(\mathbf{x}),$$

where $\boldsymbol{\Omega}$ has eigenvalues with strictly negative real part. When $p_0 = \mathcal{N}(\mathbf{m}_0, \boldsymbol{\Sigma}_0)$, the solution of the OU process is Gaussian at all times with $\mathbf{x}_t \sim \mathcal{N}(\mathbf{m}_t, \boldsymbol{\Sigma}_t)$, with $\boldsymbol{\Sigma}_t$ and $\mathbf{m}_t$ being, respectively, being the covariance and mean of the process at time t [52]. We assume that $\boldsymbol{\Sigma}_0$ is full rank, so that $\boldsymbol{\Sigma}_t$ is positive definite at all later times [52]. The covariance matrix $\boldsymbol{\Sigma}_t$ can be decomposed as $\boldsymbol{\Sigma}_t = \sum_i \sigma_{i,t}^2 \mathbf{w}_{i,t} \mathbf{w}_{i,t}^T$, where $\sigma_{i,t}$ are the eigenvalues and $\mathbf{w}_{i,t}$ are the corresponding eigenvectors. In this problem, we restrict the inferred force model to be linear, $\hat{\mathbf{f}}(\mathbf{x}) = \hat{\boldsymbol{\Omega}}\mathbf{x}$, and diffusion tensor to be a given constant $\hat{\mathbf{D}}$, perhaps previously estimated. We present an analytical form of the loss function (Eq. (6)) as a function of $\hat{\boldsymbol{\Omega}}$ in the continuous-time limit ($\Delta t \to 0$) and large sample limit ($n \to \infty$).

Continuous-time loss function. With the following theorem, we prove in App. A2 that the loss in Eq. (6) converges to a strongly convex loss for $\lambda > 0$.

Theorem I.1. *With $K = \lfloor T/\Delta t \rfloor$, when $n \to \infty$ and*

$\Delta t \to 0$, *the loss function $\mathcal{L}_{\Delta t, K}/\Delta t \to \mathcal{L}$ with*

$$\mathcal{L} = \mathrm{tr}\left((\hat{\boldsymbol{\Omega}} - \boldsymbol{\Omega})\mathbf{P}(\hat{\boldsymbol{\Omega}} - \boldsymbol{\Omega})^T + \lambda T \hat{\boldsymbol{\Omega}}\hat{\boldsymbol{\Omega}}^T \right)$$
$$+ \int_0^T \sum_{i,p} \frac{\sigma_{i,t}^2}{(\sigma_{i,t}^2 + \sigma_{p,t}^2)^2}\left(\mathbf{w}_{i,t}^T \left(\sigma_{p,t}^2(\hat{\boldsymbol{\Omega}} - \boldsymbol{\Omega}) \right.\right.$$
$$\left.\left. + \sigma_{i,t}^2(\hat{\boldsymbol{\Omega}}^T - \boldsymbol{\Omega}^T) + 2(\hat{\mathbf{D}} - \mathbf{D}) \right)\mathbf{w}_{p,t} \right)^2 dt, \quad (7)$$
$$\text{where } \mathbf{P} = \int_0^T \mathbf{m}_t \mathbf{m}_t^T.$$

For $\lambda > 0$ this loss function is strongly convex, so it has a unique minimum on $\mathbb{R}^d$.

In App. A2, we also provide a version of this theorem for the Sinkhorn divergence with entropic regularization ϵ, of which Eq. (7) is the particular case when $\epsilon \to 0$.

In the discrete-time setting, the asymptotic loss function $\mathcal{L}$ of Eq. (7) is achieved once Δt is sufficiently small to resolve all the relevant timescales. More specifically, when $\Omega_{\max}\Delta t, D\Delta t/\sigma_{\min} \ll 1$ where $\Omega_{\max}$ denotes the largest mode of $\boldsymbol{\Omega}$ and $\sigma_{\min}$ is the smallest eigenvalue of $\boldsymbol{\Sigma}_0$. The λ regularization ensures that the objective function is strongly convex, as without regularization we can face the identifiability issue. For instance, when $\lambda = 0$, if the distributions are stationary and $\mathbf{D} = \hat{\mathbf{D}}$, the minimum of the loss function $\mathcal{L} = 0$ is achieved for any matrix $\hat{\boldsymbol{\Omega}}$ that can be expressed as $\hat{\boldsymbol{\Omega}} = \boldsymbol{\Omega} + \mathbf{K}\boldsymbol{\Sigma}_0^{-1}$, where $\mathbf{K}$ is an arbitrary skew-symmetric matrix in $\mathbb{R}^{d \times d}$. We can verify that the spurious force term $\mathbf{h}(\mathbf{x}) = \mathbf{K}\boldsymbol{\Sigma}_0^{-1}\mathbf{x}$ associated with the inferred interaction matrix $\hat{\boldsymbol{\Omega}}$ satisfies Eq. (5), indicating that the true force is not uniquely identifiable.

An analytically solvable isotropic process To extend the analysis of the loss function to a non-stationary scenario, we simplify our model by considering an isotropic process, where $\boldsymbol{\Sigma}_0 = \sigma_0^2\mathbf{I}$, $\mathbf{D} = D\mathbf{I}$, and $\boldsymbol{\Omega} = \Omega_s\mathbf{I} + \boldsymbol{\Omega}_a$, with $\boldsymbol{\Omega}_a$ a skew-symmetric matrix. As a result, the covariance matrix is isotropic at all times, i.e. $\boldsymbol{\Sigma}_t = \sigma_t^2\mathbf{I}$ for all t [52]. Conveniently, for such an isotropic OU process the non-conservative and conservative forces correspond to the skew-symmetric and the symmetric parts of $\boldsymbol{\Omega}$, respectively. The non-conservative force $\boldsymbol{\Omega}_a\mathbf{x}$ generates rotations around the origin $\mathbf{x} = 0$, while the conservative part $\Omega_s\mathbf{x}$ induces inward flows.

We illustrate the PFI approach with a numerical example of an isotropic OU process in $d = 10$ dimensions, using $K = 10$ snapshots, $n = 8000$ samples and with $\lambda = 10^{-2}$. Fig. 2A shows the evolution of the true OU process projected along the two leading eigendirections of $\mathbf{P}$, with the true probability flow (dashed red lines) interpolating the successive Gaussian marginal distributions (shaded discs). The probability flow lines spiral towards the origin under the combined effect of the non-conservative and conservative forces, while diffusion is reflected in the spreading over time of the distributions. In this example, the relative strength of the non-conservative and conservative forces is 3 to 1, while the time scales of diffusion and non-conservative forces are comparable (as
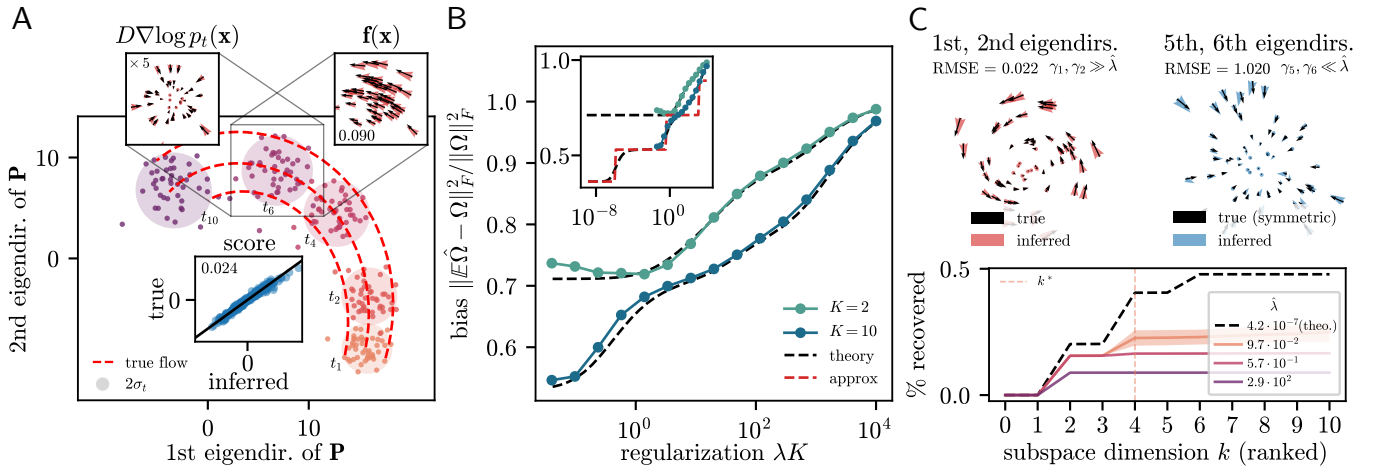
FIG. 2. **Theoretical insight for the inference of a Ornstein-Uhlenbeck process. A.** Illustration of the inference process: the inferred process samples are pushed from the true process samples at time t_i to time t_{i+1} using the PF ODE. The inferred score and inferred force field are shown (red arrows) overlaid on the true score and the true force field (dark arrows) at time t_6. The inferred force has an error of 9% (computed over the whole state-space). As shown in inset for t_6, the score inference is also accurate with an error of 2.4% **B.** Bias of the inferred interaction matrix as a function $\tilde{\lambda} = \lambda K$. In dashed lines are shown the theory (dark) and the dots correspond to numerical minimization of Eq. (6) using a pre-computed score model. In inset the bias is shown for a wider range of $\tilde{\lambda}$, and the dashed red line shows the approximate solution. **C.** In the two upper panels are shown, at $\tilde{\lambda} \simeq 10^{-1}$, projections of the inferred force field (centered in $\mathbf{x} = 0$) in the 1st and 2nd eigendirections of $\mathbf{P}$ (red arrows), and in the 5th and 6th (blue arrows). In the leading eigendirections the force field inferred matches the true force field, while as the weaker eigendirections the inference recovers the symmetric part of the true force field. In the lower panel is shown the % of true skew-symmetric interactions recovered in the k-leading eigendirections of $\mathbf{P}$. For $\tilde{\lambda} \simeq 10^{-1}$, beyond the effective dimension $k^* = 4$ the inference only infers equilibrium (here symmetric) dynamics. The parameters used are $d = 10, n = 8000, \|m_0\| = 20, \Sigma_0 = 1, D = 8, \Omega_s = 2, \Delta t = 0.05, \mathbf{\Omega}_a = 3\Omega_s\mathbf{A}$, with $\mathbf{A}$ a skew-symmetric matrix is chosen at random (Materials and Methods). The score is pre-computed with the same samples (Materials and Methods and App. C)

measured by the ratio $\tau_{\text{force}}/\tau_{\text{diff}} = D/(\Sigma_0\Omega_{\max}))$. The score estimated by sliced score-matching (Materials and Methods) is accurate (RMSE of $\sim 2.5\%$), as shown in the inset by comparing it to its analytical prediction $\nabla \log p_t(\mathbf{x}) \sim -\Sigma_t^{-1}(\mathbf{x} - \mathbf{m}_t)$. Using this score model, we infer the force using the Gaussian Wasserstein estimator to avoid the curse of dimensionality associated with the empirical Wasserstein distance [46]. At time t_6, we overlay the inferred force field on the true force field, and find that we accurately infer the force with RMSE $\sim 9\%$.

Because the covariance matrix is diagonal at all times, the skew-symmetric part can only be inferred from the motion of the mean of the distribution $\mathbf{m}_t$, which is encoded in $\mathbf{P}$. Decomposing $\mathbf{P} = \sum_i \gamma_i \mathbf{u}_i \mathbf{u}_i^T$ in terms of its eigenvalues and eigenvectors, we derive in App. A3 an analytical formula for $\hat{\mathbf{\Omega}}$, the minimum of the loss for $\lambda > 0$. This formula shows an excellent agreement with the PFI solution, as shown in Fig. 2B by plotting the bias $\|\mathbb{E}\hat{\mathbf{\Omega}} - \mathbf{\Omega}\|_F^2/\|\mathbf{\Omega}\|_F^2$ as a function of $\tilde{\lambda} = \lambda K$ for $K \in \{2, 10\}$. We can gain real insight into the role of the regularization using an approximation to $\hat{\mathbf{\Omega}}$:

$$\hat{\mathbf{\Omega}} \approx \mathbf{\Omega} - \mathbf{Q}_{\tilde{\lambda}}\mathbf{\Omega}_a\mathbf{Q}_{\tilde{\lambda}},$$

where $\mathbf{Q}_{\tilde{\lambda}} = \sum_i \chi(\gamma_i < \tilde{\lambda})\mathbf{u}_i\mathbf{u}_i^T$ is the projector onto the eigenspace of $\mathbf{P}$ having eigenvalues smaller than the penalty $\tilde{\lambda}$, with χ the indicator function. This approximation, valid for $\tilde{\lambda} \ll \sum_{j=0}^{K-1} \sigma_t^2$ and $|\tilde{\lambda}^{-1}\gamma_i - 1| \gg 1$ for all

i, is shown in inset of Fig. 2B (dashed red) in comparison with the analytical solution (dashed black). This solution suggests that the non-conservative force $\mathbf{\Omega}_a\mathbf{x}$ is inferred only in the subspace spanned by $\{\mathbf{u}_i | \gamma_i \gg \tilde{\lambda}\}$, and is set to zero in its orthogonal complement. In these remaining directions, only the conservative force is correctly estimated. This idea is further exemplified in Fig. 2C (upper panel) by showing the projections of the inferred force field on eigendirections of $\mathbf{P}$ sorted by decreasing eigenvalues γ_i. We can observe that the force field is fully estimated in the leading eigendirections, for which $\gamma_i \gg \tilde{\lambda}$, but that only the symmetric contribution is inferred when $\gamma_i \ll \tilde{\lambda}$. This observation is rationalized in Fig. 2C where we plot the fraction of recovered skew-symmetric interactions in the subspace spanned by the k leading eigenvectors of $\mathbf{P}$. This fraction is measured by $\|\mathbf{Q}_k\hat{\mathbf{\Omega}}_a\mathbf{Q}_k\|_F^2/\|\mathbf{\Omega}_a\|_F^2$, where $\mathbf{Q}_k$ is the projector on subspace spanned by the k eigenvectors associated with the k largest eigenvalues of $\mathbf{P}$. We see that beyond an effective dimension k^* the fraction plateaus, suggesting that non-conservative forces are not recovered in the remaining eigendirections. In other words, from the standpoint of inference, the time-dependent deformations of the marginal distributions in the subspace associated with the $d - k^*$ smallest eigenvalues of $\mathbf{P}$ are indistinguishable from equilibrium dynamics.

These findings highlight the role of regularization as a recovery threshold for non-equilibrium dynamics, and tak-
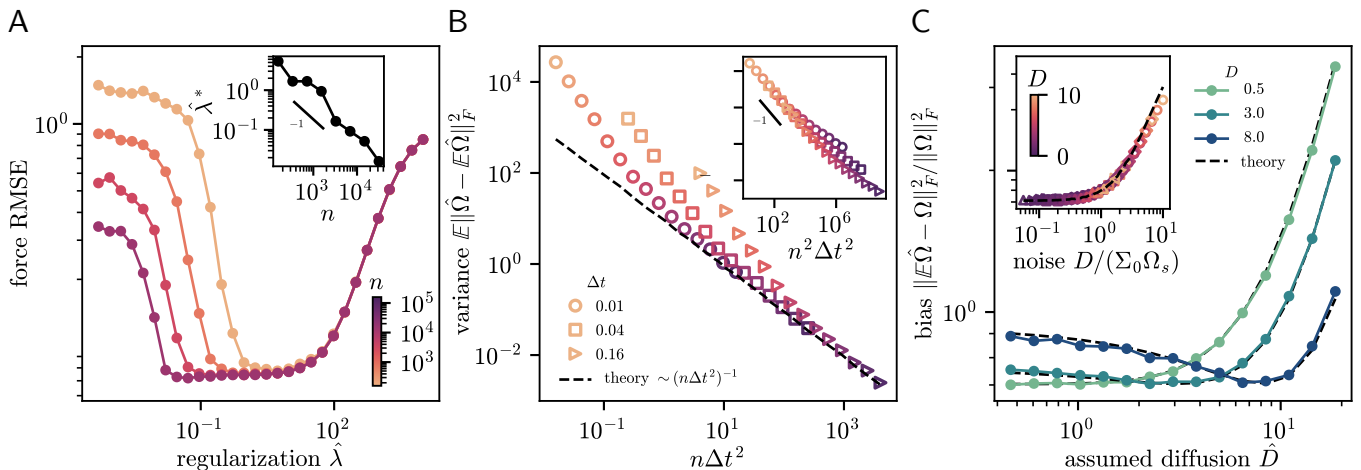
FIG. 3. **Sources of error for the inference of an Ornstein-Uhlenbeck process. A.** Bias-variance trade-off as a function of the regularization $\tilde{\lambda}$ in the relative mean square error of the force field. The inflection point of the trade-off is reached at smaller $\tilde{\lambda}$ for larger sample sizes n. **B.** Variance on the inferred interaction matrix as a function of $n\Delta t^2$, with $\Omega_s \Delta t = 0.1$, $D/\Sigma_0 \Omega_s = 4$. For various Δt the variance collapses at large n on the prediction (black dashed line). As shown in inset, at smaller n the scaling is found to be $n^2 \Delta t^2$. **C.** Bias on the inferred interaction matrix as a function of the assumed diffusion tensor $\hat{\mathbf{D}} = \hat{D}\mathbf{S}$ with $\mathbf{S}$ a semi-definite positive symmetric matrix with unit maximum eigenvalue (Materials and Methods). The bias shows a minimum when $\hat{D} = D$. When $\hat{D} = 0$ (which corresponds to fitting a deterministic model), the bias increases with D. This is shown in inset as a function of the non-dimensional strength of noise $D/\Sigma_0 \Omega_s = 3\tau_{\text{force}}/\tau_{\text{diff}}$ for different values of Σ_0 and Ω_s. With respectively increasing values for $\Sigma_0 \in \{0.5, 2, 3\}$, square, circle and right triangle markers correspond to $\Omega_s = 2$, while diamonds, left and upper triangle markers corresponds to $\Omega_s = 3$. The parameter $\|m_0\|^2/\Sigma_0$ is fixed to 400 (s.t $\|m_0\| = 20$ when $\Sigma_0 = 1$). The color map for n is shared between **A.** and **B.**. In **B.** and **C.** the regularization is $\tilde{\lambda} = 0.2$. In the three panels $K = 5$, $\Omega_a = 3\Omega_s \mathbf{A}$ and all the remaining free parameters (notably $\mathbf{A}$) in each panel are the same as Fig. 2. We use the analytical prediction for the score.

ing $\lambda \to 0$ ensures exact recovery of all non-conservative forces available in the data. However, decreasing $\tilde{\lambda}$ also incurs an increased variance coming from the finite sample size n. As shown in Fig. 3A, we observe a bias-variance trade-off in the expected relative mean square error for the interaction matrix $\mathbb{E}\|\hat{\mathbf{\Omega}} - \mathbf{\Omega}\|_F^2/\|\mathbf{\Omega}\|_F^2$. In App. A4 we derive the first-order, finite sample size correction to the continuous-time loss function, allowing us to estimate analytically the variance $\mathbb{E}\|\hat{\mathbf{\Omega}} - \mathbb{E}\hat{\mathbf{\Omega}}\|_F^2$. Given K, with all non-dimensional quantities being fixed and for n large, we predict the variance to read as $C/(n^2\Delta t)$, with C an analytical constant. This prediction is in excellent agreement with the PFI solution, as shown by the collapse in Fig. 3B as Δt is varied. Additionally, in inset we observe that at smaller sample sizes the variance scales as $(n^2\Delta t^2)^{-1}$, which we hypothesize comes from higher order terms in the finite sample size correction to the loss function. These results highlight the rather subtle balance between the regularization λ, the sample size n, and the time-step Δt, necessary to minimize the error.

In practice, this interplay strongly depends on the parametrization of the force field. For example, to go beyond linear models, the force field can be expressed as a linear combination of function basis [8] or parameterized using a neural network [24, 53]. These choices introduce implicit regularization, such as biases arising from the smoothness of the selected basis (e.g., Fourier) or activation functions in neural networks [54], and sim-

plicity biases inherent to deep neural network models [55]. Such implicit regularizations provide additional ways to constrain the solution space beyond the explicit regularization discussed here, ensuring unique solutions. For this reason, for all practical purposes, the choice of the explicit regularization is problem-specific and usually determined in an ad-hoc manner [56, 57].

Finally, our analytical solution allows us to study the error coming from the misestimation of the diffusion tensor $\hat{\mathbf{D}}$. Assuming that $\hat{\mathbf{D}} = \hat{D}\mathbf{S}$, where $\mathbf{S}$ is an arbitrary matrix in $\mathbb{S}_+^d$ (Materials and Methods) with unit maximum eigenvalue, we plot in Fig. 3C the bias $\|\mathbb{E}\hat{\mathbf{\Omega}} - \mathbf{\Omega}\|_F^2$ as a function of $\hat{D}$. These results show that the bias is minimum when $\hat{D} = D$, and that underestimating a larger intrinsic noise incurs a larger reconstruction error. This observation is rationalized using the analytical solution (App. A3), which predicts that for λ small, with K and all other non-dimensional quantities fixed, the bias at $\hat{D} = 0$ (which corresponds to fitting a deterministic model) is a known function of $\tau_{\text{force}}/\tau_{\text{diff}}$ the ratio of the timescales associated with the force and with the diffusion. This prediction agrees very well with the PFI solution, as shown in the inset of Fig. 3C for various values of Σ_0 and Ω_s. This shows that estimating $\tau_{\text{force}}/\tau_{\text{diff}}$ is an efficient way to decide whether fitting a deterministic model is sufficient ($\tau_{\text{force}}/\tau_{\text{diff}} \ll 1$) or noise is necessary ($\tau_{\text{force}}/\tau_{\text{diff}} \gtrsim 1$).

In more general cases, it may not be possible to quantify

the relative strengths of intrinsic noise and force. However, due to the Poisson nature of the chemical reactions underlying cellular processes, the intrinsic noise variance is often closely linked to the amplitude of the force [15, 16], resulting in comparable timescales for both intrinsic noise and force (i.e. $\tau_{\text{force}} \sim \tau_{\text{diff}}$). Therefore, accounting for intrinsic noise is crucial to accurately infer cellular processes from single-cell omics data. In the following, we perform numerical experiments to demonstrate how the PFI approach offers a flexible mechanism to incorporate stochasticities of arbitrary nature, and in particular molecular noise.

NUMERICAL RESULTS

In this section, we exploit the flexibility of PFI approach to infer gene regulatory networks and and model cell differentiation dynamics, incorporating molecular noise.

PFI allows accurate parameter and force estimation for stochastic reaction networks

Cellular processes are driven by an intricate array of stochastic chemical reactions [58],[59]. While techniques like flow cytometry, microscopy, and high-throughput omics provide extensive data on cellular processes, interpreting this data, their variability, and estimating reaction rate constants from it requires mechanistic models. Under the assumption that the system is well-mixed, the chemical master equation (CME) offers a detailed probabilistic representation of these stochastic reaction networks (SRNs) [60, 61]. However, the use of CME is limited in both simulation and inference tasks due to the significant computational complexity involved in solving it [62–64]. Diffusion approximations, such as the Chemical Langevin Equation (CLE), offer a computationally tractable alternative by approximating the discrete CME with a continuous diffusion process. These methods accurately capture stochastic effects at moderate molecule counts [61, 65], making them a practical and effective approximation to the CME.

However, when dealing with single-cell omics data, the stoichiometry of gene regulatory networks is unknown. In addition, simultaneous measurements of both protein and mRNA counts are generally unavailable, complicating efforts to develop detailed descriptions of the underlying stochastic regulatory networks. To address this challenge, simple coarse-grained models have been introduced that leverage the separation of timescales between transcription factor binding to regulatory DNA sites and the processes of transcription and translation [66, 67]. One such model describes the stochastic evolution of mRNA counts, denoted by $\mathbf{x} \in \mathbf{R}^d$, with d the number of genes, assuming that the transcription rate of gene i is proportional to an activation function $f_i(\mathbf{x}, V)$, $0 < f_i(\mathbf{x}, V) < 1$ with V being the reaction volume, typically that of the

nucleus. Under well-mixed assumptions, the stochastic mRNA dynamics are then be approximated by the CLE

$$d\mathbf{x} = (Vm\mathbf{f}(\mathbf{x}, V) - \ell\mathbf{x}) \, dt + \sqrt{mV\mathbf{f}(\mathbf{x}, V) + \ell\mathbf{x}} \, d\mathbf{W}, \quad (8)$$

where ℓ is the degradation rate of mRNA molecules, m is the transcription rate, and the square root is taken entry-wise. Although this model is a simplified approximation to the underlying SRNs governing gene regulation (see Materials and Methods), it has been shown to quantitatively reproduce experimental steady-state single-cell transcriptomics profiles for known gene regulatory networks [68]. By leveraging the CLE formulation in Eq. (8), the PFI approach can be readily applied to infer parameters and forces in high-dimensional SRNs. To demonstrate this, we consider the Mammalian Cortical Area Development (mCAD) gene regulatory network (see Fig. 4, $d = 5$) and use the boolODE framework [69] to compute $\mathbf{f}(\mathbf{x})$. To generate the marginal data, we conduct a detailed simulation of the mCAD stochastic reaction network using the Gillespie algorithm (Materials and Methods), producing $K = 10$ snapshots, each containing $n = 6,000$ samples.

We begin the PFI procedure by training a score network $\mathbf{s}_\phi(\mathbf{x}, t)$ to estimate the score function from the marginal data in concentration space $\mathbf{x}/V$ (Fig. S2). Using the PFI approach, we fit the Eq. (8) to the cross-sectional data by minimizing the loss function of Eq. (6). We parameterize the force using a feed-forward neural network consisting of four fully connected layers, each with 50 nodes and smooth ELU activation (see Materials and Methods). The explicit regularization parameter is set to $\lambda = 10^{-4}$. To compare the predicted and measured distributions, we apply the Sinkhorn divergence with $\epsilon = 0.1$. To assess the usefulness of the CLE description, we compare the results with those obtained by using common models for the intrinsic noise: i) additive, ii) simple state-dependent ($\sqrt{\mathbf{x}}$), and iii) deterministic (Materials and Methods). Fig. 4A shows the errors in force fields under these noise models and for increasing reaction volumes V. As expected, because the system is well-mixed, at large volumes V all the models become deterministic and perform equally well. However, across all reaction volumes, the CLE yields the most accurate force field estimates, outperforming both the state-dependent and additive noise models. Its performance degrades at small volumes when the CLE approximation breaks down.

These differences in inferred dynamics between noise models are yet better quantified by examining the estimated Jacobian matrix ($\nabla \hat{\mathbf{f}}(\mathbf{x})$), which can be used to directly infer the gene regulatory network. In Fig. 4D, we compare the average estimated Jacobian matrices for each diffusion model to the analytical Jacobian matrix (Fig. 4C). Only the CLE model accurately identifies regulatory interactions, as indicated by AUC values approaching unity, based on the precision-recall curves (Fig. 4E) [69]. Conversely, non-CLE noise models yield an AUC close to 0.5, indicating incorrect identification of interactions in the network. This result shows that while the non-CLE noise models can attain moderate errors of $\sim 10 - 20\%$ at
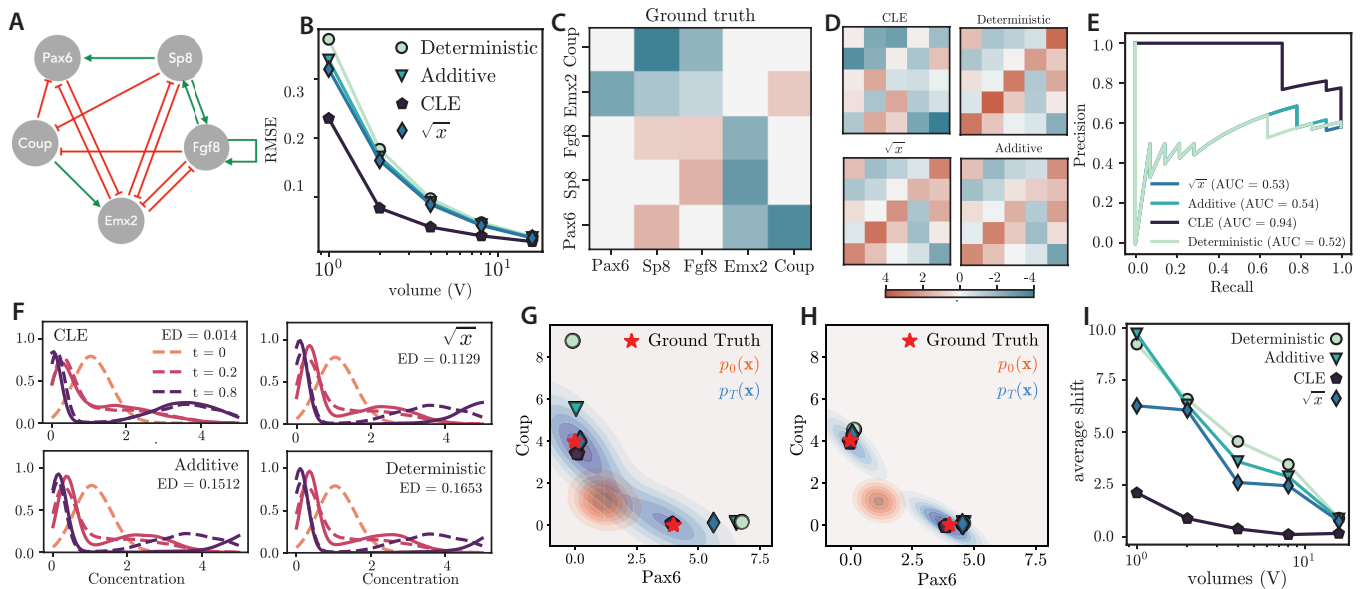
FIG. 4. **Parameter and force estimation for stochastic reaction networks. A.** mCAD gene regulatory network. Red lines denote inhibition and green arrows activation. **B.** The RMSE $\|\mathbf{f}(\mathbf{x}) - \hat{\mathbf{f}}(\mathbf{x})\|_2^2 / \|\mathbf{f}(\mathbf{x})\|_2^2$ of the inferred force shown for different compartment volumes V. The Jacobian corresponding to the true force field $\mathbf{f}(\mathbf{x})$ (**C**), with estimated Jacobians $\nabla \hat{\mathbf{f}}(\mathbf{x})$ obtained under different noise models shown in **D**. The associated precision-recall (PR) curves are displayed in **E**, with the area under the curve (AUC) values reported in the inset. **F.** Comparison of empirical marginals from the inferred diffusion process (solid) and Gillespie simulations (dashed) for $V = 4$, under various noise models (inset). The inset also reports the Energy Distance (ED) between predicted marginals and Gillespie simulations for each noise model. **G-H**: Visualization of fixed points, which are solutions to the equation $\hat{\mathbf{f}}(\mathbf{x}) - \ell\mathbf{x} = 0$, where $\hat{\mathbf{f}}(\mathbf{x})$ represents the force fields inferred under different noise models. Different markers indicate the fixed points derived from the corresponding noise models, plotted against the *Pax6* and *Coup* genes. Results are shown for two reaction volumes: $V = 4$ (**G**) and $V = 16$ (**H**). The red star represents the true fixed point (Ground Truth, $\mathbf{x}^*$), while the marginal densities at the initial state $p_0(\mathbf{x})$ (orange) and final state $p_T(\mathbf{x})$ (blue) are shown as contour plots. **I.** (**I**) The average shift $\|\mathbf{x} - \mathbf{x}^*\|_2$ as a function of reaction volume V, for different noise models.

intermediate volumes, they do so by learning a completely inaccurate regulatory network.

This observation should reflect a poor generalization performance of the non-CLE models. To test this, we ran the inferred process using initial conditions different from those in the training data (Materials and Methods). To quantify generalization, we calculated the Energy Distance (inset of Fig. 4F) between the predicted marginals from various diffusion models and the ground-truth stochastic simulations. These results show that the inferred CLE process accurately tracks the true marginals, again outperforming the other noise models. This underscores the importance of the inferred force model's accuracy in determining generalization performance.

Furthermore, we explored the dynamical behavior of these inferred force models by deterministically evolving and plotting the corresponding fixed points obtained for initial conditions sampled from the marginal distribution $\hat{p}_{t_0}(\mathbf{x})$. As molecular noise in the data increases, the fixed points for non-CLE force fields deviate from the ground truth, as shown in Fig. 4G-I. These findings complement earlier one-dimensional studies [6], which showed that multiplicative noise can shift, create, or eliminate fixed points. Our results demonstrate this effect in a high-dimensional inverse setting, underscoring the importance

of selecting appropriate noise priors to accurately capture the system's underlying dynamical properties.

Finally, in the scenario where the stoichiometry of the SRN is known, we can apply the PFI approach to estimate reaction rates in a high-dimensional setting. We consider a linear cyclic network consisting of $d = 30$ species and $R = 30$ reactions (Materials and Methods). In this constrained setting, the results are consistent with those observed for the mCAD network. The CLE approximation yields more accurate parameter estimates and better generalization performance compared to other noise models, as shown in Fig. S4.

PFI enables inference of cell differentiation dynamics with molecular noise

Cell differentiation dynamics arise from a complex interplay between deterministic mechanisms and stochastic fluctuations. However, many popular computational approaches for modeling differentiation are either purely deterministic or rely on oversimplified noise models. In this section, we examine the impact of biological noise on the predictive accuracy of widely used generative models of cellular differentiation and compare them with CLE-
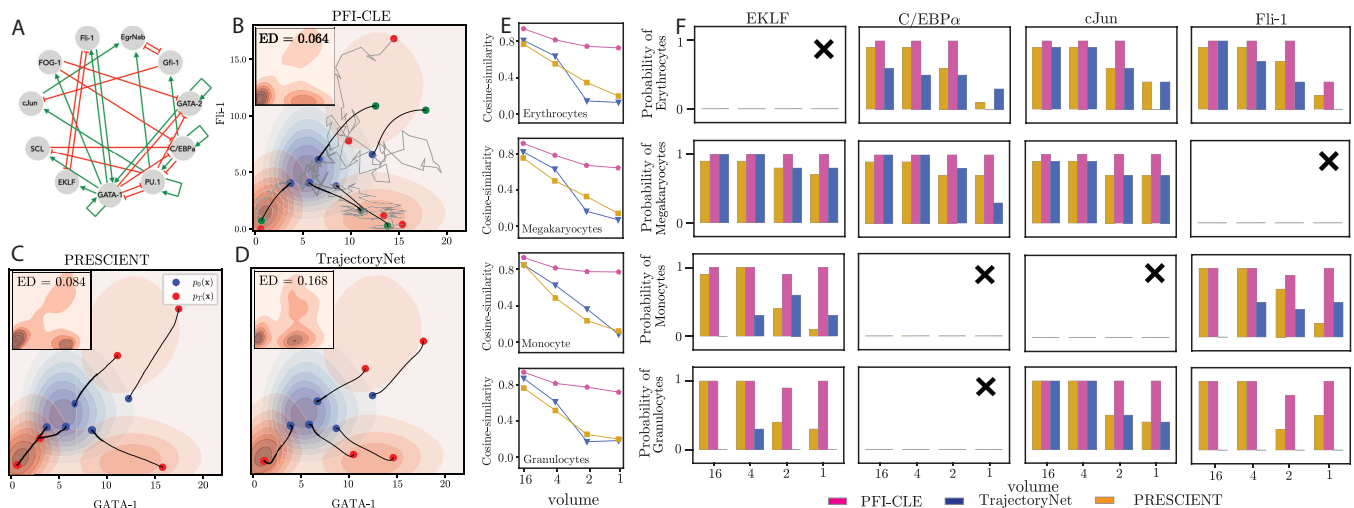
FIG. 5. **Inferred HSC differentiation dynamics and predicted perturbations. A.** HSC gene regulatory network. Red lines denote inhibition and green arrows activation. **B,C,D.** Cell differentiation trajectories using different approaches (shown in title). The marginal densities at the initial state $p_0(\mathbf{x})$ (blue) and final state $p_T(\mathbf{x})$ (orange) are shown as contour plots. In the inset, we show the reconstructed marginal at time T along with the reconstruction error (ED). **E.** Cosine similarity between inferred probability flow lines and the true CLE flow lines for four cell types (Erythrocytes, Megakaryocytes, Monocytes, and Granulocytes) under varying noise conditions (represented by volume) shown for three different approaches (PRESCIENT, TrajectoryNet, PFI). **E.** Probability of observing Erythrocytes, Megakaryocytes, Monocytes, and Granulocytes at steady state. Each panel displays the estimated probability of recovering the different cell types (rows) under specific perturbation conditions (columns). The averages are computed across varying initial conditions. The panels also show how these probabilities change with system size, V. Panels marked with a cross indicate the absence of the respective cell type under the corresponding perturbations. The results are color-coded by the approach used: TrajectoryNet (blue), PRESCIENT (gold), and Inferred Chemical Langevin model (purple).

based diffusion models inferred using the PFI approach. While various methods exist, we focus on two prominent techniques: the TrajectoryNet framework, based on dynamical optimal transport [24], and the PRESCIENT technique [53], which models diffusion through a global potential function. TrajectoryNet fits a non-autonomous force field $\mathbf{f}(\mathbf{x}, t)$ to interpolate between the marginals data with minimal kinetic energy, while PRESCIENT models differentiation dynamics as a diffusion process, with the force field $\hat{\mathbf{f}}(\mathbf{x}) = -\nabla\hat{\phi}(\mathbf{x})$ and additive noise $\hat{\mathbf{D}}(\mathbf{x}) = \sigma^2\mathbf{I}$.

We begin the comparison by generating longitudinal gene expression profiles using an expert-curated model of Myeloid Progenitor differentiation that incorporates realistic intrinsic stochasticity. This Hematopoietic Stem Cell (HSC) differentiation model includes 11 transcription factors and captures the differentiation of common myeloid progenitors (CMP) into Erythrocytes, Megakaryocytes, Monocytes, and Granulocytes. We simulate the HSC regulatory network (Fig. 5A) with the Gillespie algorithm (Materials and Methods) to generate the marginal data consisting of $K = 8$ snapshots with $n = 5000$ samples. The data is grouped into four clusters, with each cluster's average gene count profile shown in Fig. S5 for varying relations volumes. Each profile represents one of the four HSC differentiation cell types and aligns with experimentally measured mRNA data [70, 71].

We train all three models on the marginal data with

varying levels of intrinsic noise, corresponding to a reaction volume $V \in \{1, 2, 4, 16\}$. The training procedure for all three methods is discussed in Materials and Methods. To compare the inferred dynamics of the three models, we examine the individual cell trajectories generated by simulating the inferred diffusion processes. Starting from the same initial position in gene space (marked in blue), each approach predicts a different final state (marked in red) as illustrated in Fig. 5B-D. In other words, the predicted differentiated state of the same progenitor cell varies significantly between the three methods. However, despite the markedly distinct differentiation trajectories, all three methods accurately reconstruct the marginals, as shown by the low reconstruction error when measuring the distance between the predicted marginals and the data (inset Fig. 5B,C,D). For the PFI-CLE approach, we also illustrate the probability flow lines (black lines) to show how the deterministic phase velocity transports particles, and how it differs from the corresponding stochastic trajectories starting from the same initial condition. To further quantify the difference between the inferred process, we calculate the cosine similarity between the inferred probability flow lines and the CLE probability flow (PF) lines for each cell state. The probability flow of TrajectoryNet is taken to its non-autonomous force field $\mathbf{f}(\mathbf{x}, t)$, while for PRESCIENT, it is estimated as $-\nabla\hat{\phi}(\mathbf{x}) - \sigma^2\nabla\log p_t(\mathbf{x})$. As intrinsic stochasticity increases, the flow lines corresponding to TrajectoryNet and PRESCIENT diverge

significantly from the CLE flow lines in each cell state, as shown in Fig. 5E. These results illustrate that while all methods effectively interpolate between the marginal distributions, increasing intrinsic stochasticity in the data leads them to learn markedly different stochastic dynamics, as evidenced by the analysis of their probability flows and the observation individual cell trajectories.

Given the distinct dynamics learned by each approach, we next explored whether good interpolation accuracy correlates with learning the correct dynamics, and how molecular noise affects this relationship. To evaluate this, we performed perturbation studies to certify the correctness of the learned dynamics under initial conditions different from the training data (Materials and Methods). Specifically, we conduct knockdown experiments by setting the expression levels of specific genes to zero. We focus on experimentally measured outcomes for knockdowns of the genes $C/EBP\alpha$, $EKLF$, $Fli1$, and $cJun$. Experimental studies have reported that disruption of $C/EBP\alpha$ blocks the transition from the common myeloid to the granulocyte/monocyte progenitor[72], and knockdown of $cJun$ leads to loss of Monocytes lineage [71]. Similarly, disrupting $Fli1$ suppresses the Megakaryocytes cell type, while knock-down of the $EKLF$ gene leads to the absence of the Erythrocyte cell line [73]. In Fig. 5E, we report the probability of observing each cell type under various perturbation conditions. To separate the effect of the force model from the influence of noise, we perform in-silico perturbation experiments across a range of noise levels. At low noise levels, both PRESCIENT and PFI, despite using different force models, accurately predict the perturbation outcomes. However, as molecular noise increases, differences in their inferred dynamics become more pronounced, with PRESCIENT being the most affected. For instance, under high noise conditions, PRESCIENT fails to recover the Monocyte/Granulocyte lineage in multiple knockdown scenarios, whereas PFI, which accounts for molecular noise, consistently reconstructs this lineage across all noise levels. In contrast, TrajectoryNet struggles to recover the Monocyte/Granulocyte lineage even at low noise, and as stochasticity increases, its ability to reconstruct the Megakaryocyte/Erythrocyte lineage also diminishes monotonically. These findings underscore the critical role of intrinsic stochasticity and illustrate how it can impede state-of-the-art methods from accurately capturing gene regulatory interactions during differentiation. The PFI approach, by incorporating intrinsic stochasticity, enables a clearer distinction between noise and regulatory components.

DISCUSSION

In this paper, we propose PFI, an approach that transforms the problem of learning SDEs into inferring their corresponding phase-space probability flow. This is facilitated by recent advances in score-based generative modeling, which allow for efficient computation of the gradient log-probability, $\nabla \log p_t(\mathbf{x})$, from high-dimensional cross-sectional data of the time-evolving distribution $p_t(\mathbf{x})$. This reformulation dramatically simplifies optimization and, crucially, separates the impact of intrinsic noise from inferring the force field.

We first limited our analysis of the PFI problem to the analytically tractable class of Ornstein-Uhlenbeck processes. We proved that the regularization ensures a strongly convex loss with a unique global minimum in the limit of well-sampled distributions, both in time and in state-space. For an isotropic Ornstein-Uhlenbeck process, we minimized analytically this loss function, showing that the relative magnitudes of the regularization and of the time-dependent deformations of the marginals select the learnable non-equilibrium contributions to the force. While large deformations are used to learn non-conservative forces, smaller deformations are washed out by the regularization. Although this observation suggests to use a smaller regularization, we showed that the bias reduction obtained thereby trades-off with an increasing variance stemming from the finite sampling of distributions, both in time Δt and in the number of samples n. This interplay between n, Δt, and the regularization calls for careful model selection when considering complex models.

Using the same analytical solution, we subsequently showed that an inaccurate estimation of the noise strength leads to a dramatic decrease in performance when the stochastic effects are of the same order of magnitude as the force. This is of paramount importance for the inference of gene regulatory networks for which intrinsic noise is strongly correlated with the amplitude of regulation. To further explore this role of the noise model we numerically investigated more realistic models of stochastic reaction networks, using the PFI approach. Our study underscores the critical role of intrinsic noise in parameter estimation, regulatory network inference, and generalization to unseen data. An incorrect noise model can lead to spurious relationships between species, which affects the inferred probabilistic landscape [6]. Consequently, force fields based on such models exhibit poor generalization performance when tested with initial conditions different from those used during training. The PFI approach, therefore, proves to be a valuable tool for analyzing single-cell omics data, even when the stoichiometry of the reaction network is unknown.

Finally, we applied our framework to learn data-driven models of cell differentiation. To account for molecular noise, we inferred a Chemical Langevin model using the PFI approach, and compared it with popular generative models in predicting the effects of gene knockdowns in the hematopoiesis system for increase noise strength. While TrajectoryNet successfully predicts the effects of interventions when noise is negligible, it struggles when it becomes significant. On the other hand, the potential-based model PRESCIENT fails to accurately capture regulatory interactions, particularly in high-dimensional settings, even with minimal molecular noise. In contrast,

CLE-based models inferred with PFI consistently make accurate predictions, emphasizing the importance of modeling intrinsic noise to infer biological processes. Our results show that accurately interpolating the data is not enough to learn anything relevant about the underlying biological process. The interpolation needs to be guided by comprehensive biophysical models of the latent stochastic processes, and special care should be given to modeling intrinsic noise. For this purpose, the PFI approach provides a very flexible solution to incorporate more realistic intrinsic noise models in the inference of regulatory processes from single-cell omics data. In this direction, future work should aim at extending the PFI approach to account for the unobserved protein dynamics between protein production and its regulatory effects on transcription [74–78].

In this study, we primarily focus on intrinsic stochasticity in the form of molecular noise. However, extending the PFI approach to include other sources of stochasticity, like fluctuations in transcriptional rates [76, 79, 80], would be a natural step forward. More importantly, future studies should build upon the PFI framework by integrating cell death and proliferation. We believe this is a necessary step to take to successfully and reliably apply the PFI approach to real data. Given the prevalence of noise in cellular processes, our approach marks a significant step toward developing biophysically accurate, data-driven models that incorporate non-trivial stochastic effects.

II. MATERIALS AND METHODS

A. Score estimation

We employ sliced score matching [43] to estimate the score function from samples obtained through cross-sectional measurements. This estimation involves solving the following optimization problem:

$$\min_\phi \sum_{k=1}^{K} \lambda_k \mathbb{E}_{\mathbf{x}(t_k)} \mathbb{E}_{\mathbf{v} \sim p_\mathbf{v}} \left[\frac{1}{2} \left\| \mathbf{s}_\phi(\mathbf{x}(t_k), t_k) \right\|_2^2 \right.$$
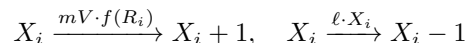$$\left. + \mathbf{v}^T \mathbf{s}_\phi(\mathbf{x}(t_k), t_k) \mathbf{v} \right]$$

where λ_k is a positive weighting function, $t \sim \mathcal{U}(0, T)$, $\mathbb{E}[\mathbf{v}] = 0$, and $\text{Cov}[\mathbf{v}] = \mathbf{I}$. We parameterize the score function $\mathbf{s}_\phi(\mathbf{x}, t) : \mathbb{R}^{d+1} \to \mathbb{R}^d$ using a fully feed-forward neural network and utilize sliced score matching [43] to estimate the score in high-dimensional spaces. During training, the weights λ are automatically tuned using the variance normalization strategy proposed in [81]. The hyperparameters of the score networks for each example are detailed in the App. C. The parameters ϕ are tuned using Adam optimizer with initial learning rate $\eta = 10^{-3}$. We evaluate the score model's accuracy by evaluating how well it reconstructs the marginal distributions (See Fig. S1)-S3).

B. Choice of matrices for the Ornstein-Uhlenbeck process

To generate a random skew-symmetric matrix we first generate a matrix $\mathbf{U} \in \mathbb{R}^{d \times d}$ with i.i.d. entries drawn uniformly at random in $[0, 1]$, and $\mathbf{e} \in \mathbb{R}^d$ a vector with i.i.d. entries drawn uniformly at random in $[0.9, 1]$. Denoting $\mathbf{W} \in \mathbb{C}^{d \times d}$ the eigenbasis of $\mathbf{U} - \mathbf{U}^T$, the matrix $\mathbf{A}$ is set to be $\mathbf{A} = \mathbf{W} \mathbf{e} \mathbf{W}^T / \max(\mathbf{e})$. The qualitative behavior shown in Figs. 2 and 3 is unchanged by repeatedly drawing new instances of $\mathbf{A}$. In Figs. 2 and 3 we used the same instance of the matrix $\mathbf{A}$. To generate a random symmetric matrix $\mathbf{S}$ we use the same approach, with the matrix $\mathbf{W}$ being the eigenbasis of $\mathbf{U} + \mathbf{U}^T$.

C. Modeling gene regulation

Under the assumption that the system is well mixed, the regulation of gene i by a set R_i of regulators obeys the following set of stochastic reactions

$$X_i \xrightarrow{mV \cdot f(R_i)} X_i + 1, \quad X_i \xrightarrow{\ell \cdot X_i} X_i - 1$$

Here, the term $mV f(R_i)$ represents the propensity associated with the reaction that produces the mRNA for gene x_i, where m denotes the transcription rate, and R_i denotes the set of regulators of node i. The term ℓX_i corresponds to the propensity of the degradation reaction, with ℓ being the degradation rate. These propensities denote the number of these reactions happening per unit of time. The non-linear function $f(R_i)$ encapsulates the regulatory interactions governing the expression of gene i, and is mediated by proteins. Given the volume of the reaction compartment, the functional form of R_i as a function of the concentration of proteins is derived from equilibrium statistical mechanics considerations [66]. In this work, we adopt its Boolean network implementation as introduced in [69].

In the absence of joint measurements of mRNA molecules and proteins, we assume that protein and mRNA levels are strongly correlated, allowing us to replace the protein regulators R_i with their mRNA counterparts. Although this assumption suggests that proteins are in quasi-steady-state with mRNA, which contrasts with observations [82, 83] of faster mRNA turnover compared to proteins [76], it still enables the recovery of single-cell RNA-seq profiles that are quantitatively comparable at steady state [68]. In practice, most gene regulatory network inference approaches ignore protein dynamics, implicitly making the similar assumption.

D. Simulation of linear stochastic reaction networks

For the linear cyclic network $X_i \xrightarrow{k_i} X_{i+1}$, rate constants k_i were generated using a logarithmic scale spanning from $10^{0.1}$ to $10^{1.5}$, distributed across $d = 30$ values,

and scaled by a factor of 0.1. Gillespie simulations were then computed using the stoichiometric matrix and the rate constants.

E. Comparison with existing methods

In the following, we describe the existing methods used to infer cell differentiation dynamics from empirical marginal distributions. We consider that $K + 1$ distributions are observed at times $t_0 \leq ... \leq t_{K+1}$, each with n samples. The PFI-CLE model is trained using the two-step PFI approach, with the force function $\mathbf{f}_\theta : \mathbb{R}^d \rightarrow \mathbb{R}^d$ represented by a feed-forward neural network. The network consists of four fully connected layers, each with 30 nodes and smooth ELU activations.

PRESCIENT: Following the original idea by Hashimoto [33], popular generative models model cellular differentiation as a diffusion process $\mathbf{x}(t)$ [53, 84], governed by the stochastic differential equation:

$$d\mathbf{x}(t) = (-\nabla \Psi(\mathbf{x}) - \ell\mathbf{x})dt + \sqrt{2\kappa^2}d\mathbf{W}(t), \qquad (9)$$

where the drift is the gradient of a potential function $\Psi(\mathbf{x})$. PRESCIENT proceeds by finding the function Ψ that minimizes the loss function

$$\mathcal{L}_{\text{PRESCIENT}} = \sum_{i=1}^{K} \left[W_2\left(\hat{p}_{t_i}(\mathbf{x}), p_{t_i}(\mathbf{x})\right)^2 + \tau \sum_{j=1}^{n} \frac{\Psi(\mathbf{x}_j)}{\kappa^2} \right].$$

The Wasserstein distance W_2 measures the difference between the observed distribution $p_{t_i}(\mathbf{x})$ and the predicted distribution $\hat{p}_{t_i}(\mathbf{x})$, and the parameter τ controls the entropic regularization. The probability distributions are fitted to the observed data by simulating the stochastic differential equation Eq. (9). The potential function $\Psi(\mathbf{x})$ is parameterized with a fully connected neural network with ELU activation function In the original study, the hyperparameters, are set to be $\kappa = 0.1$ and $\tau = 10^{-6}$, and we use the same parameters in the training of the PRESCIENT model. The potential function $\Psi(\mathbf{x})$ is parameterized with a feed-forward neural network consisting of four fully connected layers, each with 30 nodes and smooth ELU activation.

TrajectoryNet: Another popular approach for modeling cellular differentiation involves parameterizing the force field as a non-autonomous Neural ODE [24, 85], without any explicit noise model:

$$\frac{d\mathbf{x}}{dt} = \hat{\mathbf{f}}(\mathbf{x}, t).$$

Using this framework, TrajectoryNet fits a continuous normalizing flow connecting the successive distributions, enforcing an analytically tractable reference distribution $p_{t_{-1}} \sim \mathcal{N}(0, 1)$ at time t_{-1}. The loss function reads

$$\mathcal{L}_{\text{TrajectoryNet}} = -\sum_{i=0}^{K} \mathbb{E}_{p_{t_i}} \log \hat{p}_{t_i}(\mathbf{x}) + \lambda \text{regularization}.$$

The first term corresponds to the log-likelihood of the predicted distributions $\hat{p}_{t_i}(\mathbf{x})$ evaluated on the observed data $p_{t_i}(\mathbf{x})$. TrajectoryNet includes different choices for the regularization on the force field, among which are the penalization of the curvature of the force field (used in PFI) and of its kinetic energy [24]. To train TrajectoryNet we use the default parameters with the OT-inspired regularization on the kinetic energy suggested in the original study. The non-autonomous force field is modeled using a neural network with three fully connected layers, each containing 64 nodes and employing leaky ReLU activations.

F. In-silico perturbations

We conduct in-silico perturbations by simulating the inferred models from a given initial condition until a steady state is reached, with the concentration of the knocked-down gene set to zero. The models are tested with varying initial conditions derived from the training data, given by $p = (1-c)p^* + c\,\mathrm{U}[0.25, 0.5]$, to evaluate generalization. In this setup, $c = 0$ corresponds to the first marginal of the training data $p^* = \hat{p}_0(\mathbf{x})$, while $c = 1$ represents a uniform initialization of mRNA expression within the hypercube $[0.25, 0.5]^d$. We generate 10 distinct initial conditions by selecting c from a uniformly spaced grid between 0 and 1, with increments of 0.1. Cells are assigned to a specific cell state if the cosine similarity between the cell state's expression profile and the predicted expression vector is 0.95 or higher.

[1] Thattai M, van Oudenaarden A (2001) Intrinsic noise in gene regulatory networks. *Proceedings of the National Academy of Sciences* 98:8614–8619.

[2] Losick R, Desplan C (2008) Stochasticity and Cell Fate. *Science* 320:65–68.

[3] Bialek W, et al. (2012) Statistical mechanics for natural flocks of birds. *Proceedings of the National Academy of Sciences* 109:4786–4791.

[4] Jhawar J, et al. (2020) Noise-induced schooling of fish. *Nature Physics* 16:488–493 Publisher: Nature Publishing Group.

[5] Grilli J (2020) Macroecological laws describe variation and diversity in microbial communities. *Nature Communications* 11:4743.

[6] Coomer MA, Ham L, Stumpf MPH (2022) Noise distorts the epigenetic landscape and shapes cell-fate decisions.

Cell Systems 13:83–102.e6.

[7] Maheshri N, O'Shea EK (2007) Living with noisy genes: how cells function reliably with inherent variability in gene expression. *Annu. Rev. Biophys. Biomol. Struct.* 36:413–434.

[8] Frishman A, Ronceray P (2020) Learning Force Fields from Stochastic Trajectories. *Physical Review X* 10:021009.

[9] Brückner DB, Ronceray P, Broedersz CP (2020) Inferring the dynamics of underdamped stochastic systems. *Physical review letters* 125:058103.

[10] Saelens W, Cannoodt R, Todorov H, Saeys Y (2019) A comparison of single-cell trajectory inference methods. *Nature Biotechnology* 37:547–554.

[11] Schiebinger G, et al. (2019) Optimal-Transport Analysis of Single-Cell Gene Expression Identifies Developmental Trajectories in Reprogramming. *Cell* 176:928–943.e22.

[12] Brackston RD, Lakatos E, Stumpf MP (2018) Transition state characteristics during cell differentiation. *PLoS computational biology* 14:e1006405.

[13] Weinreb C, Wolock S, Tusi BK, Socolovsky M, Klein AM (2018) Fundamental limits on dynamic inference from single-cell snapshots. *Proceedings of the National Academy of Sciences* 115:E2467–E2476.

[14] Gardiner C (2009) *Stochastic Methods*, 0172-7389 (Springer-Verlag Berlin Heidelberg) Vol. 13.

[15] Ahlmann-Eltze C, Huber W (2023) Comparison of transformations for single-cell RNA-seq data. *Nature Methods* 20:665–672.

[16] Choudhary S, Satija R (2022) Comparison and evaluation of statistical error models for scRNA-seq. *Genome Biology* 23:27.

[17] Pérez García L, Donlucas Pérez J, Volpe G, V. Arzola A, Volpe G (2018) High-performance reconstruction of microscopic force fields from Brownian trajectories. *Nature Communications* 9:5166.

[18] Ferretti F, Chardès V, Mora T, Walczak AM, Giardina I (2020) Building General Langevin Models from Discrete Datasets. *Physical Review X* 10:031018.

[19] Kutoyants YA (2004) *Statistical Inference for Ergodic Diffusion Processes*, Springer Series in Statistics (Springer, London).

[20] Yang KD, Uhler C (2018) Scalable unbalanced optimal transport using generative adversarial networks. *arXiv preprint arXiv:1810.11447*.

[21] Schiebinger G (2021) Reconstructing developmental landscapes and trajectories from single-cell data. *Current Opinion in Systems Biology* 27:100351.

[22] Zhang S, Afanassiev A, Greenstreet L, Matsumoto T, Schiebinger G (2021) Optimal transport analysis reveals trajectories in steady-state systems. *PLOS Computational Biology* 17:e1009466.

[23] Bunne C, et al. (2023) Learning single-cell perturbation responses using neural optimal transport. *Nature Methods* pp 1–10.

[24] Tong A, Huang J, Wolf G, Van Dijk D, Krishnaswamy S (2020) *Trajectorynet: A dynamic optimal transport network for modeling cellular dynamics* (PMLR), pp 9526–9536.

[25] Chizat L, Zhang S, Heitz M, Schiebinger G (2022) Trajectory Inference via Mean-field Langevin in Path Space. *Advances in Neural Information Processing Systems* 35:16731–16742.

[26] Lavenant H, Zhang S, Kim YH, Schiebinger G (2023) Towards a mathematical theory of trajectory inference.

[27] Bunne C, Hsieh YP, Cuturi M, Krause A (2023) *The Schrödinger Bridge between Gaussian Measures has a Closed Form* (PMLR), pp 5802–5833.

[28] Ocone A, Haghverdi L, Mueller NS, Theis FJ (2015) Reconstructing gene regulatory dynamics from high-dimensional single-cell snapshot data. *Bioinformatics* 31:i89–i96.

[29] Matsumoto H, et al. (2017) Scode: an efficient regulatory network inference algorithm from single-cell rna-seq during differentiation. *Bioinformatics* 33:2314–2321.

[30] Sanchez-Castillo M, Blanco D, Tienda-Luna IM, Carrion M, Huang Y (2018) A bayesian framework for the inference of gene regulatory networks from time and pseudo-time series data. *Bioinformatics* 34:964–970.

[31] Zhou P, Bocci F, Li T, Nie Q (2024) Spatial transition tensor of single cells. *Nature Methods* pp 1–10.

[32] Gillespie DT (2000) The chemical Langevin equation. *The Journal of Chemical Physics* 113:297–306.

[33] Hashimoto T, Gifford D, Jaakkola T (2016) *Learning Population-Level Diffusions with Generative RNNs* (PMLR), pp 2417–2426.

[34] Li X, Wong TKL, Chen RT, Duvenaud D (2020) *Scalable gradients for stochastic differential equations* (PMLR), pp 3870–3882.

[35] Maoutsa D, Reich S, Opper M (2020) Interacting particle solutions of fokker–planck equations through gradient–log–density estimation. *Entropy* 22:802.

[36] Boffi NM, Vanden-Eijnden E (2023) Probability flow solution of the Fokker–Planck equation. *Machine Learning: Science and Technology* 4:035012 Publisher: IOP Publishing.

[37] Hyvärinen A (2005) Estimation of Non-Normalized Statistical Models by Score Matching. *Journal of Machine Learning Research* 6:695–709.

[38] Atkinson K (1991) *An introduction to numerical analysis* (John wiley & sons).

[39] Chen RT, Rubanova Y, Bettencourt J, Duvenaud DK (2018) Neural ordinary differential equations. *Advances in neural information processing systems* 31.

[40] Grathwohl W, Chen RT, Bettencourt J, Sutskever I, Duvenaud D (2018) *FFJORD: Free-Form Continuous Dynamics for Scalable Reversible Generative Models*.

[41] Rubanova Y, Chen RT, Duvenaud DK (2019) Latent ordinary differential equations for irregularly-sampled time series. *Advances in neural information processing systems* 32.

[42] Song Y, et al. (2020) *Score-Based Generative Modeling through Stochastic Differential Equations*.

[43] Song Y, Garg S, Shi J, Ermon S (2020) *Sliced Score Matching: A Scalable Approach to Density and Score Estimation* (PMLR), pp 574–584.

[44] Wang J, Xu L, Wang E (2008) Potential landscape and flux framework of nonequilibrium networks: robustness, dissipation, and coherence of biochemical oscillations. *Proceedings of the National Academy of Sciences* 105:12271–12276.

[45] Wang J, Zhang K, Xu L, Wang E (2011) Quantifying the waddington landscape and biological paths for development and differentiation. *Proceedings of the National Academy of Sciences* 108:8257–8262.

[46] Genevay A, Peyre G, Cuturi M (2018) *Learning Generative Models with Sinkhorn Divergences* (PMLR), pp

1608–1617.

[47] Genevay A, Chizat L, Bach F, Cuturi M, Peyré G (2019) *Sample complexity of Sinkhorn divergences* (PMLR), pp 1574–1583.

[48] Rippl T, Munk A, Sturm A (2016) Limit laws of the empirical Wasserstein distance: Gaussian distributions. *Journal of Multivariate Analysis* 151:90–109.

[49] Yuan B, et al. (2021) Cellbox: interpretable machine learning for perturbation biology with application to the design of cancer combination therapy. *Cell systems* 12:128–140.

[50] La Manno G, et al. (2018) Rna velocity of single cells. *Nature* 560:494–498.

[51] Bergen V, Lange M, Peidli S, Wolf FA, Theis FJ (2020) Generalizing rna velocity to transient cell states through dynamical modeling. *Nature biotechnology* 38:1408–1414.

[52] Särkkä S, Solin A (2019) *Applied stochastic differential equations* (Cambridge University Press) Vol. 10.

[53] Yeo GHT, Saksena SD, Gifford DK (2021) Generative modeling of single-cell time series with prescient enables prediction of cell trajectories with interventions. *Nature communications* 12:3222.

[54] Mishra S, Molinaro R (2022) Estimates on the generalization error of physics-informed neural networks for approximating a class of inverse problems for pdes. *IMA Journal of Numerical Analysis* 42:981–1022.

[55] Pérez GV, Louis AA, Camargo CQ (2019) *Deep learning generalizes because the parameter-function map is biased towards simple functions.*

[56] Bishop CM, Nasrabadi NM (2006) *Pattern recognition and machine learning* (Springer) Vol. 4.

[57] Hastie T, Tibshirani R, Friedman JH, Friedman JH (2009) *The elements of statistical learning: data mining, inference, and prediction* (Springer) Vol. 2.

[58] McAdams HH, Arkin A (1997) Stochastic mechanisms in gene expression. *Proceedings of the National Academy of Sciences* 94:814–819.

[59] Raser JM, O'shea EK (2005) Noise in gene expression: origins, consequences, and control. *Science* 309:2010–2013.

[60] Gillespie DT (1992) A rigorous derivation of the chemical master equation. *Physica A: Statistical Mechanics and its Applications* 188:404–425.

[61] Schnoerr D, Sanguinetti G, Grima R (2017) Approximation and inference methods for stochastic biochemical kinetics—a tutorial review. *Journal of Physics A: Mathematical and Theoretical* 50:093001 Publisher: IOP Publishing.

[62] Fröhlich F, Kaltenbacher B, Theis FJ, Hasenauer J (2017) Scalable parameter estimation for genome-scale biochemical reaction networks. *PLoS computational biology* 13:e1005331.

[63] Zechner C, Unger M, Pelet S, Peter M, Koeppl H (2014) Scalable inference of heterogeneous reaction kinetics from pooled single-cell recordings. *Nature methods* 11:197–202.

[64] Drovandi CC, Pettitt AN, Faddy MJ (2011) Approximate bayesian computation using indirect inference. *Journal of the Royal Statistical Society Series C: Applied Statistics* 60:317–337.

[65] Mozgunov P, et al. (2018) A review of the deterministic and diffusion approximations for stochastic chemical reaction networks. *Reaction Kinetics, Mechanisms and Catalysis* 123:289–312.

[66] Marbach D, et al. (2010) Revealing strengths and weaknesses of methods for gene network inference. *Proceedings of the National Academy of Sciences* 107:6286–6291 Publisher: Proceedings of the National Academy of Sciences.

[67] Bower JM, Bolouri H (2001) *Computational Modeling of Genetic and Biochemical Networks* (The MIT Press).

[68] Dibaeinia P, Sinha S (2020) Sergio: a single-cell expression simulator guided by gene regulatory networks. *Cell systems* 11:252–271.

[69] Pratapa A, Jalihal AP, Law JN, Bharadwaj A, Murali TM (2020) Benchmarking algorithms for gene regulatory network inference from single-cell transcriptomic data. *Nature Methods* 17:147–154.

[70] Pronk CJ, et al. (2007) Elucidation of the phenotypic, functional, and molecular topography of a myeloerythroid progenitor cell hierarchy. *Cell stem cell* 1:428–442.

[71] Krumsiek J, Marr C, Schroeder T, Theis FJ (2011) Hierarchical differentiation of myeloid progenitors is encoded in the transcription factor network. *PloS one* 6:e22649.

[72] Zhang P, et al. (2004) Enhancement of hematopoietic stem cell repopulating capacity and self-renewal in the absence of the transcription factor $c/ebp\alpha$. *Immunity* 21:853–863.

[73] Nuez B, Michalovich D, Bygrave A, Ploemacher R, Grosveld F (1995) Defective haematopoiesis in fetal liver resulting from inactivation of the eklf gene. *Nature: international weekly journal of science* 375:316–318.

[74] Josić K, López JM, Ott W, Shiau L, Bennett MR (2011) Stochastic Delay Accelerates Signaling in Gene Networks. *PLOS Computational Biology* 7:e1002264 Publisher: Public Library of Science.

[75] Bratsun D, Volfson D, Tsimring LS, Hasty J (2005) Delay-induced stochastic oscillations in gene regulation. *Proceedings of the National Academy of Sciences* 102:14593–14598 Publisher: Proceedings of the National Academy of Sciences.

[76] Herbach U, Bonnaffoux A, Espinasse T, Gandrillon O (2017) Inferring gene regulatory networks from single-cell data: a mechanistic approach. *BMC Systems Biology* 11:105.

[77] Herbach U (2021) Gene regulatory network inference from single-cell data using a self-consistent proteomic field. arXiv:2109.14888 [q-bio].

[78] Ventre E, Herbach U, Espinasse T, Benoit G, Gandrillon O (2023) One model fits all: Combining inference and simulation of gene regulatory networks. *PLOS Computational Biology* 19:e1010962 Publisher: Public Library of Science.

[79] Ham L, Brackston RD, Stumpf MP (2020) Extrinsic noise and heavy-tailed laws in gene expression. *Physical review letters* 124:108101.

[80] Gorin G, Vastola JJ, Fang M, Pachter L (2022) Interpretable and tractable models of transcriptional noise for the rational design of single-molecule quantification experiments. *Nature Communications* 13:7620.

[81] Maddu S, Sturm D, Müller CL, Sbalzarini IF (2022) Inverse dirichlet weighting enables reliable training of physics informed neural networks. *Machine Learning: Science and Technology* 3:015026.

[82] Abreu RdS, Penalva LO, Marcotte EM, Vogel C (2009) Global signatures of protein and mRNA expression levels. *Molecular BioSystems* 5:1512–1526 Publisher: The Royal Society of Chemistry.

[83] Shahrezaei V, Swain PS (2008) Analytical distributions for stochastic gene expression. *Proceedings of the National Academy of Sciences* 105:17256–17261.

[84] Sisan DR, Halter M, Hubbard JB, Plant AL (2012) Predicting rates of cell state change caused by stochastic fluctuations using a data-driven landscape model. *Proceedings of the National Academy of Sciences* 109:19262–19267.

[85] Sha Y, Qiu Y, Zhou P, Nie Q (2024) Reconstructing growth and dynamic trajectories from single-cell transcriptomics data. *Nature Machine Intelligence* 6:25–39.

[86] Gillespie DT (1976) A general method for numerically simulating the stochastic time evolution of coupled chemical reactions. *Journal of computational physics* 22:403–434.

[87] Gillespie DT (1977) Exact stochastic simulation of coupled chemical reactions. *The journal of physical chemistry* 81:2340–2361.

[88] Giacomantonio CE, Goodhill GJ (2010) A boolean model of the gene regulatory network underlying mammalian cortical area development. *PLoS computational biology* 6:e1000936.

[89] Welling M, Teh YW (2011) *Bayesian learning via stochastic gradient Langevin dynamics* (Citeseer), pp 681–688.

[90] Song Y, Ermon S (2019) *Generative Modeling by Estimating Gradients of the Data Distribution* (Curran Associates, Inc.), Vol. 32.

Appendix A: Analytical results for the Ornstein-Uhlenbeck process

1. Notation and preliminaries

We focus on the d-dimensional Ornstein-Uhlenbeck process. The true process reads as follows:

$$d\mathbf{x} = \mathbf{\Omega}\mathbf{x}dt + \sqrt{2\mathbf{D}}d\mathbf{W}, \text{ with } \mathbf{x}_0 \sim p_0(\mathbf{x}).$$

When $p_0 = \mathcal{N}(\mathbf{m}_0, \mathbf{\Sigma}_0)$, the solution of this stochastic differential equation is Gaussian at all times with

$$\mathbf{x}_t \sim \mathcal{N}(\mathbf{m}_t, \mathbf{\Sigma}_t),$$
$$\text{where } \mathbf{m}_t = e^{\mathbf{\Omega}t}\mathbf{m}_0, \ \mathbf{\Sigma}_t = e^{\mathbf{\Omega}t}\mathbf{\Sigma}_0 e^{\mathbf{\Omega}^T t} + \int_0^t e^{\mathbf{\Omega}(t-s)}2\mathbf{D}e^{\mathbf{\Omega}^T(t-s)}ds. \tag{A1}$$

We require that the eigenvalues of $\mathbf{\Omega}$ have a strictly negative real part. We can see that if $\mathbf{\Omega}$ is a normal matrix (i.e. it commutes with its transpose), the diffusion matrix $\mathbf{D}$ and the initial condition $\mathbf{\Sigma}_0$ are isotropic (proportional to identity) and the initial condition $\mathbf{m}_0 = 0$, then the evolution of the marginals of the Ornstein-Uhlenbeck process is independent of the skew-symmetric part of $\mathbf{\Omega}$ with

$$\mathbf{m}_t = 0, \ \mathbf{\Sigma}_t = \Sigma_0 e^{(\mathbf{\Omega}+\mathbf{\Omega}^T)t} + 2D\int_0^t e^{(\mathbf{\Omega}+\mathbf{\Omega}^T)(t-s)}ds.$$

In that case, since neither the first or second moment depend on the skew-symmetric part, it is impossible to infer it by only exploiting time deformations of the marginal distributions. We see here that in such a scenario the marginal distributions are not at steady-state but the true skew-symmetric part of the interaction matrix can't be uniquely identified. However, as soon as $\mathbf{m}_0 \neq 0$ this degeneracy is lifted and the skew-symmetric terms can be identified. To illustrate this we further simplify the true process by taking the symmetric part of $\mathbf{\Omega}$ also isotropic. With $\mathbf{\Sigma}_0 = \Sigma_0 \mathbf{I}$, isotropic diffusion D and interaction matrix $\mathbf{\Omega} = \Omega_s \mathbf{I} + \mathbf{\Omega}_a$ with $\mathbf{\Omega}_a$ skew-symmetric, the covariance matrix at time t is always isotropic and reads

$$\Sigma_t = \Sigma_0 e^{2\Omega_s t} + D\frac{e^{2\Omega_s t}}{\Omega_s}\left[1 - e^{-2\Omega_s t}\right].$$

The distribution associated with the true process is denoted $p_t(\mathbf{x})$. The inferred process is solution of the following Fokker-Planck equation on the interval $[t_k, t_k + \Delta t[$ with initial condition $\hat{p}_{t_k} = p_{t_k}$

$$\frac{\partial \hat{p}_t(\mathbf{x})}{\partial t} = -\nabla \cdot \left(\hat{\mathbf{\Omega}}\mathbf{x}\hat{p}_t(\mathbf{x}) - \hat{\mathbf{D}}\nabla\hat{p}_t(\mathbf{x})\right).$$

The inferred process is then also Gaussian, with for $t \in [t_k, t_k + \Delta t[$

$$\hat{\mathbf{x}}_t \sim \mathcal{N}(\hat{\mathbf{m}}_t, \hat{\mathbf{\Sigma}}_t),$$
$$\text{where } \hat{\mathbf{m}}_t = e^{\hat{\mathbf{\Omega}}(t-t_k)}\mathbf{m}_{t_k}, \ \hat{\mathbf{\Sigma}}_t = e^{\hat{\mathbf{\Omega}}(t-t_k)}\mathbf{\Sigma}_{t_k}e^{\hat{\mathbf{\Omega}}^T(t-t_k)} + \int_{t_k}^t e^{\hat{\mathbf{\Omega}}(t-t_k-s)}2\hat{\mathbf{D}}e^{\hat{\mathbf{\Omega}}^T(t-t_k-s)}ds. \tag{A2}$$

In practice n i.i.d samples $\{\mathbf{x}_{k,t_i}, 1 \leq k < n\}$ are measured at each time t_i from the true marginals, such that we only have access to an empirical estimator of p_{t_i}. Additionally, we evolve the inferred process from the observed samples $\{\mathbf{x}_{k,t_i}, 1 \leq k < n, 0 \leq i \leq K\}$ using the probability flow ODE, assuming the score is known. We only perform one integration step, and the update equation reads

$$\hat{\mathbf{x}}_{k,\Delta t} = \left(\mathbf{I} + \Delta t\hat{\mathbf{\Omega}}\right)\mathbf{x}_{k,0} + \Delta t\hat{\mathbf{D}}\hat{\mathbf{\Sigma}}_0^{-1}\left(\mathbf{x}_{k,0} - \mathbf{m}_0\right). \tag{A3}$$

As a result, the inferred process used in the inference is an approximation of the exact inferred process Eq. (A2). At first order in Δt, the exact Eq. (A2) and the approximate inferred processes Eq. (A3) have the same mean and covariance, but differ at higher orders. In the $\Delta t \to 0$ limit that we consider only the first order will be relevant, such that approximate and exact inferred process will lead to the same continuous-time loss.

2. Continuous-time loss for the Wasserstein distance

a. *Theorem for the continuous-time loss.* When $n \to +\infty$ and $\Delta t \to 0$, the loss function $\mathcal{L}_{\Delta t, K}/\Delta t \to \mathcal{L}$ with

$$\mathcal{L} = \mathrm{tr}\left((\hat{\boldsymbol{\Omega}} - \boldsymbol{\Omega})^T (\hat{\boldsymbol{\Omega}} - \boldsymbol{\Omega}) \mathbf{P} + \lambda T \hat{\boldsymbol{\Omega}} \hat{\boldsymbol{\Omega}}^T \right) \tag{A4}$$
$$+ \int_0^T \sum_{i,p} \frac{\sigma_{i,t}^2}{(\sigma_{i,t}^2 + \sigma_{p,t}^2)^2} \left(\mathbf{w}_{i,t}^T \left(\sigma_{p,t}^2 (\hat{\boldsymbol{\Omega}} - \boldsymbol{\Omega}) + \sigma_{i,t}^2 (\hat{\boldsymbol{\Omega}}^T - \boldsymbol{\Omega}^T) + 2(\hat{\mathbf{D}} - \mathbf{D}) \right) \mathbf{w}_{p,t} \right)^2 dt,$$

where

$$\mathbf{P} = \int_0^T \mathbf{m}_t \mathbf{m}_t^T.$$

For $\lambda > 0$ this loss function is strongly convex, such that is has a unique minimum on $\mathbb{R}^{d \times d}$ which is also global.

Proof. We consider that $n \to \infty$ such that $\hat{p}_{t_i}$ and p_{t_i} are Gaussian distributions. The loss function reads as follows

$$\mathcal{L}_{\Delta t, K} = \sum_{i=1}^K \mathcal{W}_2^2(\hat{p}_{t_i}, p_{t_i}) + \lambda K \Delta t^2 \|\hat{\boldsymbol{\Omega}}\|_F^2 = \sum_{i=0}^{K-1} \mathcal{W}_2^2(\hat{p}_{t_i + \Delta t}, p_{t_i + \Delta t}) + \lambda K \Delta t^2 \|\hat{\boldsymbol{\Omega}}\|_F^2. \tag{A5}$$

Let's consider the first term $t_0 = 0$ in the above sum. We have $p_{\Delta t} \sim \mathcal{N}(\mathbf{m}_{\Delta t}, \boldsymbol{\Sigma}_{\Delta t})$ and $\hat{p}_{\Delta t} \sim \mathcal{N}(\hat{\mathbf{m}}_{\Delta t}, \hat{\boldsymbol{\Sigma}}_{\Delta t})$, and the Wasserstein distance between both distribution reads

$$\mathcal{W}_2^2(\hat{p}_{\Delta t}, p_{\Delta t}) = \|\hat{\mathbf{m}}_{\Delta t} - \mathbf{m}_{\Delta t}\|^2 + \mathrm{tr}(\hat{\boldsymbol{\Sigma}}_{\Delta t}) + \mathrm{tr}(\boldsymbol{\Sigma}_{\Delta t}) - 2\mathrm{tr}\left(\left(\boldsymbol{\Sigma}_{\Delta t}^{1/2} \hat{\boldsymbol{\Sigma}}_{\Delta t} \boldsymbol{\Sigma}_{\Delta t}^{1/2} \right)^{1/2} \right).$$

We denote the small time step expansion of the covariance matrices as

$$\boldsymbol{\Sigma}_{\Delta t} = \boldsymbol{\Sigma}_0 + \Delta t \mathbf{B} + \Delta t^2 \mathbf{C} + o(\Delta t^2),$$
$$\hat{\boldsymbol{\Sigma}}_{\Delta t} = \boldsymbol{\Sigma}_0 + \Delta t \hat{\mathbf{B}} + \Delta t^2 \hat{\mathbf{C}} + o(\Delta t^2), \tag{A6}$$

where at all orders the matrices are symmetric. We then search for $\mathbf{U}, \mathbf{V}$ and $\mathbf{Z}$ such that $\boldsymbol{\Sigma}_{\Delta t}^{1/2} = \mathbf{U} + \Delta t \mathbf{V} + \Delta t^2 \mathbf{Z} + o(\Delta t^2)$. By squaring this guess and using the uniqueness of the Taylor expansion we find the conditions

$$\mathbf{U} = \boldsymbol{\Sigma}_0^{1/2}, \mathbf{UV} + \mathbf{VU} = \mathbf{B}, \mathbf{UZ} + \mathbf{ZU} + \mathbf{V}^2 = \mathbf{C}.$$

$\mathbf{V}$ is solution of a Lyapunov equation, for which the solution can be written as an integral. Denoting $\boldsymbol{\Sigma}_0^{1/2} = \sum_i \sigma_i \mathbf{w}_i \mathbf{w}_i^T = \sum_i \sigma_i \mathbf{z}_i$ with $\mathbf{z}_i = \mathbf{w}_i \mathbf{w}_i^T$ the solution reads

$$\mathbf{V} = \int_0^\infty e^{-\boldsymbol{\Sigma}_0^{1/2} t} \mathbf{B} e^{-\boldsymbol{\Sigma}_0^{1/2} t} dt = \sum_{i,j} \mathbf{z}_i \int_0^\infty e^{-\sigma_i t} \mathbf{B} e^{-\sigma_j t} \mathbf{z}_j = \sum_{i,j} \frac{1}{\sigma_i + \sigma_j} \mathbf{z}_i \mathbf{B} \mathbf{z}_j.$$

We then have

$$\mathbf{V}^2 = \sum_{i,j,p} \frac{1}{(\sigma_i + \sigma_p)(\sigma_p + \sigma_j)} \mathbf{z}_i \mathbf{B} \mathbf{z}_p \mathbf{B} \mathbf{z}_j,$$

which allows us to compute

$$\mathbf{Z} = \sum_{i,j} \frac{1}{\sigma_i + \sigma_j} \mathbf{z}_i \mathbf{C} \mathbf{z}_j - \sum_{i,j,p} \frac{1}{(\sigma_i + \sigma_j)(\sigma_p + \sigma_j)(\sigma_i + \sigma_p)} \mathbf{z}_i \mathbf{B} \mathbf{z}_p \mathbf{B} \mathbf{z}_j.$$

We introduce the notation 't.' for transpose, and we can compute the expansion in powers of Δt of $\boldsymbol{\Sigma}_{\Delta t}^{1/2} \hat{\boldsymbol{\Sigma}}_{\Delta t} \boldsymbol{\Sigma}_{\Delta t}^{1/2}$

$$\boldsymbol{\Sigma}_{\Delta t}^{1/2} \hat{\boldsymbol{\Sigma}}_{\Delta t} \boldsymbol{\Sigma}_{\Delta t}^{1/2} = \boldsymbol{\Sigma}_0^2 + \Delta t \boldsymbol{\Sigma}_0^{1/2} \hat{\mathbf{B}} \boldsymbol{\Sigma}_0^{1/2} + \Delta t \left(\boldsymbol{\Sigma}_0^{3/2} \sum_{i,j} \frac{1}{\sigma_i + \sigma_j} \mathbf{z}_i \mathbf{B} \mathbf{z}_j + \mathrm{t.} \right)$$

$$+ \Delta t^2 \left(\boldsymbol{\Sigma}_0^{3/2} \left[\sum_{i,j} \frac{1}{\sigma_i + \sigma_j} \mathbf{z}_i \mathbf{C} \mathbf{z}_j - \sum_{i,j,p} \frac{1}{(\sigma_i + \sigma_j)(\sigma_p + \sigma_j)(\sigma_i + \sigma_p)} \mathbf{z}_i \mathbf{B} \mathbf{z}_p \mathbf{B} \mathbf{z}_j \right] + \mathrm{t.} \right)$$

$$+ \Delta t^2 \left(\boldsymbol{\Sigma}_0^{1/2} \hat{\mathbf{B}} \sum_{i,j} \frac{1}{\sigma_i + \sigma_j} \mathbf{z}_i \mathbf{B} \mathbf{z}_j + \mathrm{t.} \right) + \Delta t^2 \boldsymbol{\Sigma}_0^{1/2} \hat{\mathbf{C}} \boldsymbol{\Sigma}_0^{1/2} + \Delta t^2 \sum_{i,j,p,l} \frac{1}{(\sigma_p + \sigma_l)(\sigma_i + \sigma_j)} \mathbf{z}_i \mathbf{B} \mathbf{z}_j \boldsymbol{\Sigma}_0 \mathbf{z}_p \mathbf{B} \mathbf{z}_l.$$

Following the same approach, we now perform the expansion in powers of Δt of $\left(\boldsymbol{\Sigma}_{\Delta t}^{1/2}\hat{\boldsymbol{\Sigma}}_{\Delta t}\boldsymbol{\Sigma}_{\Delta t}^{1/2}\right)^{1/2}$

$$
\begin{aligned}
\left(\boldsymbol{\Sigma}_{\Delta t}^{1/2}\hat{\boldsymbol{\Sigma}}_{\Delta t}\boldsymbol{\Sigma}_{\Delta t}^{1/2}\right)^{1/2} =\ & \boldsymbol{\Sigma}_0 + \Delta t \sum_{i,j}\frac{\sigma_i\sigma_j}{\sigma_i^2+\sigma_j^2}\mathbf{z}_i\hat{\mathbf{B}}\mathbf{z}_j + \Delta t\left(\sum_{i,j}\frac{\sigma_i^3}{(\sigma_i+\sigma_j)(\sigma_i^2+\sigma_j^2)}\mathbf{z}_i\mathbf{B}\mathbf{z}_j + \text{t.}\right)\\
& + \Delta t^2\left(\sum_{i,j}\frac{\sigma_i^3}{(\sigma_i+\sigma_j)(\sigma_i^2+\sigma_j^2)}\mathbf{z}_i\mathbf{C}\mathbf{z}_j + \text{t.}\right)\\
& - \Delta t^2\left(\sum_{i,j}\frac{\sigma_i^3}{(\sigma_i+\sigma_j)(\sigma_i+\sigma_p)(\sigma_p+\sigma_j)(\sigma_i^2+\sigma_j^2)}\mathbf{z}_i\mathbf{B}\mathbf{z}_p\mathbf{B}\mathbf{z}_j + \text{t.}\right)\\
& + \Delta t^2\sum_{i,j}\frac{\sigma_i\sigma_j}{\sigma_i^2+\sigma_j^2}\mathbf{z}_i\hat{\mathbf{C}}\mathbf{z}_j + \Delta t^2\left(\sum_{i,j,p}\frac{\sigma_i}{(\sigma_j+\sigma_p)(\sigma_i^2+\sigma_j^2)}\mathbf{z}_i\hat{\mathbf{B}}\mathbf{z}_p\mathbf{B}\mathbf{z}_j + \text{t.}\right)\\
& + \Delta t^2\sum_{i,j,p}\frac{\sigma_p^2}{(\sigma_i+\sigma_p)(\sigma_p+\sigma_i)(\sigma_i^2+\sigma_j^2)}\mathbf{z}_i\mathbf{B}\mathbf{z}_p\mathbf{B}\mathbf{z}_j - \Delta t^2\mathbf{E},
\end{aligned}
\tag{A7}
$$

where $\mathbf{E}$ is given by

$$
\begin{aligned}
\mathbf{E} =\ & \sum_{i,j}\frac{1}{\sigma_i^2+\sigma_j^2}\mathbf{z}_i\left(\sum_{p,l}\frac{\sigma_p\sigma_l}{\sigma_p^2+\sigma_l^2}\mathbf{z}_p\hat{\mathbf{B}}\mathbf{z}_l + \left(\sum_{p,l}\frac{\sigma_p^3}{(\sigma_p+\sigma_l)(\sigma_p^2+\sigma_l^2)}\mathbf{z}_p\mathbf{B}\mathbf{z}_l + \text{t.}\right)\right)^2\mathbf{z}_j\\
=\ & \sum_{i,j,p}\frac{\sigma_i\sigma_j\sigma_p^2}{(\sigma_i^2+\sigma_j^2)(\sigma_i^2+\sigma_p^2)(\sigma_p^2+\sigma_j^2)}\mathbf{z}_i\hat{\mathbf{B}}\mathbf{z}_p\hat{\mathbf{B}}\mathbf{z}_j + \sum_{i,j,p}\frac{(\sigma_i^3+\sigma_p^3)(\sigma_p^3+\sigma_j^3)}{(\sigma_i^2+\sigma_j^2)(\sigma_i^2+\sigma_p^2)(\sigma_p^2+\sigma_j^2)(\sigma_i+\sigma_p)(\sigma_j+\sigma_p)}\mathbf{z}_i\mathbf{B}\mathbf{z}_p\mathbf{B}\mathbf{z}_j\\
& + \left(\sum_{i,j,p}\frac{\sigma_i\sigma_p(\sigma_j^3+\sigma_p^3)}{(\sigma_i^2+\sigma_j^2)(\sigma_i^2+\sigma_p^2)(\sigma_p^2+\sigma_j^2)(\sigma_p+\sigma_j)}\mathbf{z}_i\hat{\mathbf{B}}\mathbf{z}_p\mathbf{B}\mathbf{z}_j + \text{t.}\right)
\end{aligned}
$$

We then take the trace of Eq. (A7), and using the circular property of the trace and $\sum_i\mathbf{z}_i = \mathbf{I}$ we are left with

$$
\begin{aligned}
\operatorname{tr}\left(\left(\boldsymbol{\Sigma}_{\Delta t}^{1/2}\hat{\boldsymbol{\Sigma}}_{\Delta t}\boldsymbol{\Sigma}_{\Delta t}^{1/2}\right)^{1/2}\right) =\ & \operatorname{tr}(\boldsymbol{\Sigma}_0) + \frac{\Delta t}{2}\left(\operatorname{tr}(\mathbf{B}+\hat{\mathbf{B}})\right) + \frac{\Delta t^2}{2}\left(\operatorname{tr}(\mathbf{C}+\hat{\mathbf{C}})\right)\\
& + \frac{\Delta t^2}{2}\sum_{i,p}\left(\frac{1}{(\sigma_i+\sigma_p)\sigma_i}\operatorname{tr}(\hat{\mathbf{B}}\mathbf{z}_p\mathbf{B}\mathbf{z}_i + \text{t.}) + \frac{\sigma_p^2}{\sigma_i^2(\sigma_i+\sigma_p)^2}\operatorname{tr}(\mathbf{B}\mathbf{z}_p\mathbf{B}\mathbf{z}_i) - \frac{1}{(\sigma_i+\sigma_p)^2}\operatorname{tr}(\mathbf{B}\mathbf{z}_p\mathbf{B}\mathbf{z}_i)\right)\\
& - \Delta t^2\operatorname{tr}(\mathbf{E}),
\end{aligned}
\tag{A8}
$$

where we also have

$$
\operatorname{tr}(\mathbf{E}) = \frac{1}{2}\sum_{i,p}\left(\frac{(\sigma_i^3+\sigma_p^3)^2}{\sigma_i^2(\sigma_i^2+\sigma_p^2)^2(\sigma_i+\sigma_p)^2}\operatorname{tr}(\mathbf{B}\mathbf{z}_p\mathbf{B}\mathbf{z}_i) + \frac{\sigma_p^2}{(\sigma_i^2+\sigma_p^2)^2}\operatorname{tr}(\hat{\mathbf{B}}\mathbf{z}_p\hat{\mathbf{B}}\mathbf{z}_i) + \frac{\sigma_p(\sigma_i^3+\sigma_p^3)}{\sigma_i(\sigma_i^2+\sigma_p^2)^2(\sigma_i+\sigma_p)}\operatorname{tr}(\hat{\mathbf{B}}\mathbf{z}_p\mathbf{B}\mathbf{z}_i + \text{t.})\right)
$$

For $\mathbf{M}$ and $\mathbf{N}$ two symmetric positive definite matrices, we have that $\mathbf{M}\mathbf{N}$ is similar to $\mathbf{N}^{1/2}\left(\mathbf{M}\mathbf{N}\right)\mathbf{N}^{-1/2} = \mathbf{N}^{1/2}\mathbf{M}\mathbf{N}^{1/2}$. With the same argument, $\mathbf{M}\mathbf{N}$ is similar to $\mathbf{M}^{1/2}\mathbf{N}\mathbf{M}^{1/2}$, such that $\mathbf{M}^{1/2}\mathbf{N}\mathbf{M}^{1/2}$ and $\mathbf{N}^{1/2}\mathbf{M}\mathbf{N}^{1/2}$ are similar. As a result, $\boldsymbol{\Sigma}_{\Delta t}^{1/2}\hat{\boldsymbol{\Sigma}}_{\Delta t}\boldsymbol{\Sigma}_{\Delta t}^{1/2}$ and $\hat{\boldsymbol{\Sigma}}_{\Delta t}^{1/2}\boldsymbol{\Sigma}_{\Delta t}\hat{\boldsymbol{\Sigma}}_{\Delta t}^{1/2}$ are similar, and we can write

$$
\operatorname{tr}\left(\left(\boldsymbol{\Sigma}_{\Delta t}^{1/2}\hat{\boldsymbol{\Sigma}}_{\Delta t}\boldsymbol{\Sigma}_{\Delta t}^{1/2}\right)^{1/2}\right) = \operatorname{tr}\left(\left(\hat{\boldsymbol{\Sigma}}_{\Delta t}^{1/2}\boldsymbol{\Sigma}_{\Delta t}\hat{\boldsymbol{\Sigma}}_{\Delta t}^{1/2}\right)^{1/2}\right).
$$

At all order in Δt this equality holds, such that the terms $\hat{\mathbf{B}}$ and $\mathbf{B}$ as well as the terms $\hat{\mathbf{C}}$ and $\mathbf{C}$ should be exchangeable in Eq. (A8). This symmetry is clearly respected at the order Δt^2 for $\mathbf{C}$ and $\hat{\mathbf{C}}$, but it is not striking for $\hat{\mathbf{B}}$ and $\mathbf{B}$. Let's illustrate that this symmetry holds: using the circular property of the trace we see that the trace terms are symmetric in the indices i and p, and we can reorganize the sums

$$
\sum_{i,p}\frac{\sigma_i^2\sigma_p^4}{\sigma_i^2(\sigma_i^2+\sigma_p^2)^2(\sigma_i+\sigma_p)^2}\operatorname{tr}(\mathbf{B}\mathbf{z}_p\mathbf{B}\mathbf{z}_i) = \sum_{i,p}\frac{\sigma_i^6}{\sigma_i^2(\sigma_i^2+\sigma_p^2)^2(\sigma_i+\sigma_p)^2}\operatorname{tr}(\mathbf{B}\mathbf{z}_p\mathbf{B}\mathbf{z}_i),
$$

which allows us to find that

$$\sum_{i,p} \left(\frac{\sigma_p^2}{\sigma_i^2(\sigma_i + \sigma_p)^2} - \frac{1}{(\sigma_i + \sigma_p)^2} - \frac{(\sigma_i^3 + \sigma_p^3)^2}{\sigma_i^2(\sigma_i^2 + \sigma_p^2)^2(\sigma_i + \sigma_p)^2} \right) \operatorname{tr}(\mathbf{B}\mathbf{z}_p\mathbf{B}\mathbf{z}_i) = -\sum_{i,p} \frac{\sigma_p^2}{(\sigma_i^2 + \sigma_p^2)^2} \operatorname{tr}(\mathbf{B}\mathbf{z}_p\mathbf{B}\mathbf{z}_i).$$

Finally, using the following identity

$$\sum_{i,p} \frac{\sigma_p\sigma_i^3}{\sigma_i(\sigma_i^2 + \sigma_p^2)^2(\sigma_i + \sigma_p)} \operatorname{tr}(\hat{\mathbf{B}}\mathbf{z}_p\mathbf{B}\mathbf{z}_i + \text{t.}) = \sum_{i,p} \frac{\sigma_p^2\sigma_i^2}{\sigma_i(\sigma_i^2 + \sigma_p^2)^2(\sigma_i + \sigma_p)} \operatorname{tr}(\hat{\mathbf{B}}\mathbf{z}_p\mathbf{B}\mathbf{z}_i + \text{t.}),$$

we can rewrite Eq. (A8) as

$$\operatorname{tr}\left(\left(\boldsymbol{\Sigma}_{\Delta t}^{1/2}\hat{\boldsymbol{\Sigma}}_{\Delta t}\boldsymbol{\Sigma}_{\Delta t}^{1/2} \right)^{1/2} \right) = \operatorname{tr}(\boldsymbol{\Sigma}_0) + \frac{\Delta t}{2}\left(\operatorname{tr}(\mathbf{B} + \hat{\mathbf{B}}) \right) + \frac{\Delta t^2}{2}\left(\operatorname{tr}(\mathbf{C} + \hat{\mathbf{C}}) \right)$$
$$+ \frac{\Delta t^2}{2} \sum_{i,p} \left(\frac{\sigma_i}{(\sigma_i + \sigma_p)(\sigma_i^2 + \sigma_p^2)} \operatorname{tr}(\hat{\mathbf{B}}\mathbf{z}_p\mathbf{B}\mathbf{z}_i + \text{t.}) - \frac{\sigma_p^2}{(\sigma_i^2 + \sigma_p^2)^2} \operatorname{tr}(\mathbf{B}\mathbf{z}_p\mathbf{B}\mathbf{z}_i + \hat{\mathbf{B}}\mathbf{z}_p\hat{\mathbf{B}}\mathbf{z}_i) \right).$$

With this equality we see that the symmetry for the role of $\hat{\mathbf{B}}$ and $\mathbf{B}$ is also respected. We can perform one last simplification since we have

$$\sum_{i,p} \frac{\sigma_i}{(\sigma_i + \sigma_p)(\sigma_i^2 + \sigma_p^2)} \operatorname{tr}(\hat{\mathbf{B}}\mathbf{z}_p\mathbf{B}\mathbf{z}_i + \text{t.}) = \sum_{i,p} \frac{\sigma_p^2}{(\sigma_i^2 + \sigma_p^2)^2} \operatorname{tr}(\hat{\mathbf{B}}\mathbf{z}_p\mathbf{B}\mathbf{z}_i + \text{t.}),$$

such that the trace reads

$$\operatorname{tr}\left(\left(\boldsymbol{\Sigma}_{\Delta t}^{1/2}\hat{\boldsymbol{\Sigma}}_{\Delta t}\boldsymbol{\Sigma}_{\Delta t}^{1/2} \right)^{1/2} \right) = \operatorname{tr}(\boldsymbol{\Sigma}_0) + \frac{\Delta t}{2}\left(\operatorname{tr}(\mathbf{B} + \hat{\mathbf{B}}) \right) + \frac{\Delta t^2}{2}\left(\operatorname{tr}(\mathbf{C} + \hat{\mathbf{C}}) \right)$$
$$+ \frac{\Delta t^2}{2} \sum_{i,p} \frac{\sigma_p^2}{(\sigma_i^2 + \sigma_p^2)^2} \operatorname{tr}(\hat{\mathbf{B}}\mathbf{z}_p\mathbf{B}\mathbf{z}_i + \mathbf{B}\mathbf{z}_p\hat{\mathbf{B}}\mathbf{z}_i - \mathbf{B}\mathbf{z}_p\mathbf{B}\mathbf{z}_i - \hat{\mathbf{B}}\mathbf{z}_p\hat{\mathbf{B}}\mathbf{z}_i),$$

which leaves us with

$$\operatorname{tr}\left(\left(\boldsymbol{\Sigma}_{\Delta t}^{1/2}\hat{\boldsymbol{\Sigma}}_{\Delta t}\boldsymbol{\Sigma}_{\Delta t}^{1/2} \right)^{1/2} \right) = \operatorname{tr}(\boldsymbol{\Sigma}_0) + \frac{\Delta t}{2}\left(\operatorname{tr}(\mathbf{B} + \hat{\mathbf{B}}) \right) + \frac{\Delta t^2}{2}\left(\operatorname{tr}(\mathbf{C} + \hat{\mathbf{C}}) \right) - \frac{\Delta t^2}{2} \sum_{i,p} \frac{\sigma_p^2}{(\sigma_i^2 + \sigma_p^2)^2} \operatorname{tr}\left((\hat{\mathbf{B}} - \mathbf{B})\mathbf{z}_p(\hat{\mathbf{B}} - \mathbf{B})\mathbf{z}_i \right)$$
$$\text{(A9)}$$

The covariance part of the Wasserstein loss is $\operatorname{tr}(\boldsymbol{\Sigma}_{\Delta t}) + \operatorname{tr}(\boldsymbol{\Sigma}_{\Delta t}) - 2\operatorname{tr}((\boldsymbol{\Sigma}_{\Delta t}^{1/2}\hat{\boldsymbol{\Sigma}}_{\Delta t}\boldsymbol{\Sigma}_{\Delta t}^{1/2})^{1/2})$. Using the small time-step expansion of the covariance matrices Eq. (A6), only the last term Eq. (A9) remains and the Wasserstein loss now reads

$$\mathcal{W}_2^2(\hat{p}_{\Delta t}, p_{\Delta t}) = \Delta t^2 \|(\hat{\boldsymbol{\Omega}} - \boldsymbol{\Omega})\mathbf{m}_0\|^2 + \Delta t^2 \sum_{i,p} \frac{\sigma_p^2}{(\sigma_i^2 + \sigma_p^2)^2} \operatorname{tr}\left((\hat{\mathbf{B}} - \mathbf{B})\mathbf{z}_p(\hat{\mathbf{B}} - \mathbf{B})\mathbf{z}_i \right) + o(\Delta t^2).$$

Using Eq. (A1) we find that $\mathbf{B} = \boldsymbol{\Omega}\boldsymbol{\Sigma}_0 + \boldsymbol{\Sigma}_0\boldsymbol{\Omega}^T + 2\mathbf{D}$ and $\mathbf{B} = \hat{\boldsymbol{\Omega}}\boldsymbol{\Sigma}_0 + \boldsymbol{\Sigma}_0\hat{\boldsymbol{\Omega}}^T + 2\hat{\mathbf{D}}$ such that

$$\mathcal{W}_2^2(\hat{p}_{\Delta t}, p_{\Delta t}) = \Delta t^2 \|(\hat{\boldsymbol{\Omega}} - \boldsymbol{\Omega})\mathbf{m}_0\|^2 + \Delta t^2 \sum_{i,p} \frac{\sigma_p^2}{(\sigma_i^2 + \sigma_p^2)^2} \left(\mathbf{w}_i^T \left((\hat{\boldsymbol{\Omega}} - \boldsymbol{\Omega})\boldsymbol{\Sigma}_0 + \boldsymbol{\Sigma}_0(\hat{\boldsymbol{\Omega}} - \boldsymbol{\Omega})^T + 2(\hat{\mathbf{D}} - \mathbf{D}) \right) \mathbf{w}_p \right)^2 + o(\Delta t^2).$$

Doing this for every term of the sum in Eq. (A5) we recognize a Riemann sum such that in the limit $\Delta t \to 0$ the loss $\mathcal{L}_{\Delta t, K_{\Delta t}}/\Delta t \to \mathcal{L}$ were $\mathcal{L}$ is given by Eq. (A4). The function $\mathbf{X} \longmapsto \operatorname{tr}(\mathbf{X}\mathbf{A}\mathbf{X}^T\mathbf{B})$ is convex for any $\mathbf{A}, \mathbf{B}$ positive semi-definite matrices. Since $\mathbf{m}_i\mathbf{m}_i^T, \mathbf{z}_i$ for $1 \le i \le d$ are positive semi-definite, $\hat{\boldsymbol{\Omega}} \longmapsto \hat{\boldsymbol{\Omega}} - \boldsymbol{\Omega}$ and $\hat{\boldsymbol{\Omega}} \longmapsto (\hat{\boldsymbol{\Omega}} - \boldsymbol{\Omega})\boldsymbol{\Sigma}_0 + \boldsymbol{\Sigma}_0(\hat{\boldsymbol{\Omega}} - \boldsymbol{\Omega})^T + 2(\hat{\mathbf{D}} - \mathbf{D})$ are affine functions of $\hat{\boldsymbol{\Omega}}$, we can conclude that the mean and covariance part of the loss are convex functions of $\hat{\boldsymbol{\Omega}}$. The function $\hat{\boldsymbol{\Omega}} \longmapsto \|\hat{\boldsymbol{\Omega}}\|_F^2$ being strongly convex and the sum of convex and strongly convex functions being strongly convex, so is the loss function. $\square$

b. Generalization to the Sinkhorn divergence. We can extend this approach to a more general version of the loss replacing the Wasserstein distance by the Sinkhorn divergence. The Sinkhorn divergence between the inferred and true processes with entropic regularization $\epsilon \geq 0$ reads as follows

$$\mathcal{S}_{2,\epsilon}(\hat{p}_{\Delta t}, p_{\Delta t}) = \mathcal{W}_{2,\epsilon}^2(\hat{p}_{\Delta t}, p_{\Delta t}) - \frac{1}{2}\left(\mathcal{W}_{2,\epsilon}^2(p_{\Delta t}, p_{\Delta t}) + \mathcal{W}_{2,\epsilon}^2(\hat{p}_{\Delta t}, \hat{p}_{\Delta t})\right).$$

where $\mathcal{W}_{2,\epsilon}^2$ denotes the entropy-regularized Wasserstein distance, which reads for Gaussian distributions

$$\mathcal{W}_{2,\epsilon}(\hat{p}_{\Delta t}, p_{\Delta t}) = \|\hat{\mathbf{m}}_{\Delta t} - \mathbf{m}_{\Delta t}\|^2 + \text{tr}(\hat{\mathbf{\Sigma}}_{\Delta t}) + \text{tr}(\mathbf{\Sigma}_{\Delta t}) + \frac{\epsilon}{2}\log\det\left(\mathbf{I} + \frac{1}{2}\mathbf{M}_\epsilon(\hat{\mathbf{\Sigma}}_{\Delta t}, \mathbf{\Sigma}_{\Delta t})\right) - \frac{\epsilon}{2}\text{tr}\left(\mathbf{M}_\epsilon(\hat{\mathbf{\Sigma}}_{\Delta t}, \mathbf{\Sigma}_{\Delta t})\right),$$

$$\text{where } \mathbf{M}_\epsilon(\hat{\mathbf{\Sigma}}_{\Delta t}, \mathbf{\Sigma}_{\Delta t}) = -\mathbf{I} + \left(\mathbf{I} + \frac{16}{\epsilon^2}\mathbf{\Sigma}_{\Delta t}^{1/2}\hat{\mathbf{\Sigma}}_{\Delta t}\mathbf{\Sigma}_{\Delta t}^{1/2}\right)^{1/2}.$$

We can perform a similar expansion in powers of Δt for this loss, using the matrix square root expansion illustrated above, along with the matrix logarithm expansion. This latter expansion around a matrix $\mathbf{X}$ reads as follows, with $u \to 0$

$$\log(\mathbf{X} + u\mathbf{Y}) = \log\mathbf{X} + \int_0^\infty dt\left(u(\mathbf{X} + t\mathbf{I})^{-1}\mathbf{Y}(\mathbf{X} + t\mathbf{I})^{-1} - u^2(\mathbf{X} + t\mathbf{I})^{-1}\mathbf{Y}(\mathbf{X} + t\mathbf{I})^{-1}\mathbf{Y}(\mathbf{X} + t\mathbf{I})^{-1}\right) + O(u^3).$$

Thanks to the similarity of the matrices $\mathbf{\Sigma}_{\Delta t}^{1/2}\hat{\mathbf{\Sigma}}_{\Delta t}\mathbf{\Sigma}_{\Delta t}^{1/2}$ and $\hat{\mathbf{\Sigma}}_{\Delta t}^{1/2}\mathbf{\Sigma}_{\Delta t}\hat{\mathbf{\Sigma}}_{\Delta t}^{1/2}$ we can directly simplify many terms in the expansion to account for the symmetry between inferred and true matrices. The calculations are nonetheless much lengthier than for the Wasserstein distance, and we only provide the end result for the continuous-time loss

$$\mathcal{L}_\epsilon = \text{tr}\left((\hat{\mathbf{\Omega}} - \mathbf{\Omega})^T(\hat{\mathbf{\Omega}} - \mathbf{\Omega})\mathbf{P} + \lambda T\hat{\mathbf{\Omega}}\hat{\mathbf{\Omega}}^T\right)$$
$$+ \int_0^T \sum_{i,p} \frac{\xi_{i,t}}{(\xi_{i,t} + \xi_{p,t})^2}\left(\mathbf{w}_{i,t}^T\left(\sigma_{p,t}^2(\hat{\mathbf{\Omega}} - \mathbf{\Omega}) + \sigma_{i,t}^2(\hat{\mathbf{\Omega}}^T - \mathbf{\Omega}^T) + 2(\mathbf{S} - \mathbf{D})\right)\mathbf{w}_{p,t}\right)^2 dt,$$

where

$$\xi_{i,t} = \sqrt{\epsilon^2/16 + \sigma_{i,t}^4}, \quad \mathbf{P} = \int_0^T \mathbf{m}_t\mathbf{m}_t^T.$$

Similarly to the case of the Wasserstein loss, this loss function is strongly convex. We verify that when $\epsilon \to 0$ we recover the continuous-time loss for the Wasserstein distance Eq. (A5). In the limit of an isotropic process $\sigma_{i,t} = \sigma_{p,t}$ for all i, p and at all times t the part corresponding to the covariances simplifies and the loss reads

$$\mathcal{L}_\epsilon = \text{tr}\left((\hat{\mathbf{\Omega}} - \mathbf{\Omega})^T(\hat{\mathbf{\Omega}} - \mathbf{\Omega})\mathbf{P} + \frac{q}{4}(\hat{\mathbf{\Omega}} + \hat{\mathbf{\Omega}}^T - 2\Omega_s\mathbf{I})^2 + r(\hat{\mathbf{\Omega}} + \hat{\mathbf{\Omega}}^T - 2\Omega_s\mathbf{I})(\mathbf{S} - D\mathbf{I}) + \lambda T\hat{\mathbf{\Omega}}\hat{\mathbf{\Omega}}^T\right), \quad \text{(A10)}$$

where

$$q = \int_0^T \frac{\sigma_t^4}{\sqrt{\epsilon^2/16 + \sigma_t^4}}dt \text{ and } r = \int_0^T \frac{\sigma_t^2}{\sqrt{\epsilon^2/16 + \sigma_t^4}}dt.$$

3. Results in the isotropic case

The matrix $\mathbf{P}$ is symmetric positive semi-definite since

$$\mathbf{x}^T\mathbf{P}\mathbf{x} = \int_0^T \mathbf{x}^T e^{\mathbf{\Omega}t}\mathbf{m}_0\mathbf{m}_0^T e^{\mathbf{\Omega}^T t}\mathbf{x}dt = \int_0^T \|\mathbf{x}^T e^{\mathbf{\Omega}t}\mathbf{m}_0\|^2 dt \geq 0.$$

This matrix is therefore diagonalizable in an orthogonal basis of vectors $\mathbf{U} = (\mathbf{u}_1, ..., \mathbf{u}_d)$ of $\mathbb{R}^d$, such that $\mathbf{P} = \mathbf{U}\mathbf{\Gamma}\mathbf{U}^T$ where $\mathbf{\Gamma} = \text{diag}(\gamma_1, ..., \gamma_d)$, and $\gamma_1 \geq \gamma_2 \geq ... \geq \gamma_d$.

a. *Solution with regularization.* For $\lambda > 0$, the minimum value of the loss Eq. (A10) is attained for

$$\hat{\mathbf{\Omega}} = \mathbf{\Omega} - \sum_{i,j} \frac{\tilde{\lambda}\tilde{q}^{-1}\eta_{ij}(1 + \gamma_i\tilde{\lambda}^{-1}) + \omega_{ij}(1 + \gamma_i\tilde{q}^{-1})}{\tilde{q}^{-1}\tilde{\lambda}^{-1}\gamma_i\gamma_j + \Gamma_+(\gamma_i + \gamma_j) + 1} \mathbf{u}_i\mathbf{u}_j^T.$$

with

$$\tilde{\lambda} = \lambda T, \ \tilde{q} = q + \tilde{\lambda}, \ \Gamma_+ = \frac{1}{2}(\tilde{\lambda}^{-1} + \tilde{q}^{-1}).$$

and $\omega_{ij} = \mathbf{u}_i^T\mathbf{\Omega}_a\mathbf{u}_j$ and $\eta_{ij} = \mathbf{u}_i^T(\mathbf{\Omega}_s\mathbf{I} + r(\hat{\mathbf{D}} - D\mathbf{I})/\tilde{\lambda})\mathbf{u}_j$.

Proof. The loss function $\mathcal{L}$ is a polynomial of the coefficients of A and is therefore infinitely differentiable over $\mathbb{R}^d$. We can find the minimum by writing the first order optimality condition

$$2(\hat{\mathbf{\Omega}} - \mathbf{\Omega})\mathbf{P} + q(\hat{\mathbf{\Omega}}^T + \hat{\mathbf{\Omega}} - 2\mathbf{\Omega}_s\mathbf{I}) + 2r(\hat{\mathbf{D}} - D\mathbf{I}) + 2\lambda T\hat{\mathbf{\Omega}} = 0.$$

Let's for now assume that $\lambda > 0$. We introduce $\mathbf{C} = \hat{\mathbf{\Omega}} - \mathbf{\Omega}$, and we would like to rewrite this equation in the form of a linear system displaying only $\mathbf{C}$. To do that we separate symmetric and skew-symmetric parts. We denote $\mathbf{Y} = \mathbf{\Omega}_s\mathbf{I} + r(\hat{\mathbf{D}} - D\mathbf{I})/(\lambda T)$ such that

$$\mathbf{CP} + \mathbf{PC}^T + q(\mathbf{C} + \mathbf{C}^T) + \lambda T(\mathbf{C} + \mathbf{C}^T) + 2\lambda T\mathbf{Y} = 0, \tag{A11}$$
$$\mathbf{CP} - \mathbf{PC}^T + \lambda T(\mathbf{C} - \mathbf{C}^T) + 2\lambda T\mathbf{\Omega}_a = 0. \tag{A12}$$

We denote $\tilde{q} = q + \lambda T$ and $\tilde{\lambda} = \lambda T$, and we can solve for $\mathbf{C}^T$ in the first equation and then replace it in the second equation. We use the fact that the matrix $(\tilde{q}\mathbf{I} + \mathbf{P})$ is symmetric positive definite and hence invertible

$$\mathbf{C}^T = -(\tilde{q}\mathbf{I} + \mathbf{P})^{-1}\left(\mathbf{C}(\tilde{q}\mathbf{I} + \mathbf{P}) + 2\tilde{\lambda}\mathbf{Y}\right).$$

Using the eigendecomposition of $\mathbf{P}$ and using the Woodbury formula we find

$$(\tilde{q}\mathbf{I} + \mathbf{P})^{-1} = \tilde{q}^{-1}\mathbf{I} - \tilde{q}^{-2}\mathbf{U}(\mathbf{\Gamma}^{-1} + \mathbf{U}^T\mathbf{U}\tilde{q}^{-1})^{-1}\mathbf{U}^T.$$

Since $\mathbf{\Gamma}$ is diagonal and $\mathbf{U}^T\mathbf{U} = \mathbf{I}$, $\mathbf{\Gamma}^{-1} + \mathbf{U}^T\mathbf{U}\tilde{q}^{-1}$ is diagonal and invertible and $(\mathbf{\Gamma}^{-1} + \mathbf{U}^T\mathbf{U}\tilde{q}^{-1})_{jj} = 1 + \gamma_j\tilde{q}^{-1}/\gamma_j$ for all $1 \le j \le d$, which gives

$$(\tilde{q}\mathbf{I} + \mathbf{P})^{-1} = \tilde{q}^{-1}\mathbf{I} - \sum_{j=1}^{d}\frac{\gamma_j\tilde{q}^{-2}}{1 + \gamma_j\tilde{q}^{-1}}\mathbf{u}_j\mathbf{u}_j^T = \tilde{q}^{-1}(\mathbf{I} - \tilde{q}^{-1}\tilde{\mathbf{P}}), \tag{A13}$$

where we have introduced the matrix $\tilde{\mathbf{P}}$ that reads

$$\tilde{\mathbf{P}} = \sum_{i=1}^{d}\frac{\gamma_i}{1 + \gamma_i\tilde{q}^{-1}}\mathbf{u}_i\mathbf{u}_i^T.$$

Using Eq. (A13) we have $\mathbf{P}(\tilde{q}\mathbf{I} + \mathbf{P})^{-1} = \tilde{q}^{-1}\tilde{\mathbf{P}}$ such that

$$-\mathbf{PC}^T - \tilde{\lambda}\mathbf{C}^T = (1 - \tilde{\lambda}\tilde{q}^{-1})\tilde{q}^{-1}\tilde{\mathbf{P}}\left(\mathbf{C}(\tilde{q}\mathbf{I} + \mathbf{P}) + 2\tilde{\lambda}\mathbf{Y}\right) + \tilde{\lambda}\mathbf{C} + \tilde{\lambda}\tilde{q}^{-1}\mathbf{CP} + 2\tilde{\lambda}\tilde{q}^{-1}\tilde{\lambda}\mathbf{Y}.$$

Injecting it in Eq. (A12) we are left with

$$(1 + \tilde{\lambda}\tilde{q}^{-1})\mathbf{CP} + 2\tilde{\lambda}\mathbf{C} + (1 - \tilde{\lambda}\tilde{q}^{-1})\tilde{\mathbf{P}}\mathbf{C} + \tilde{q}^{-1}(1 - \tilde{\lambda}\tilde{q}^{-1})\tilde{\mathbf{P}}\mathbf{CP} + 2\tilde{\lambda}\tilde{q}^{-1}(1 - \tilde{\lambda}\tilde{q}^{-1})\tilde{\mathbf{P}}\mathbf{Y} + 2\tilde{\lambda}\tilde{q}^{-1}\tilde{\lambda}\mathbf{Y} + 2\tilde{\lambda}\mathbf{\Omega}_a = 0. \tag{A14}$$

We introduce $\Gamma_- = (\tilde{\lambda}^{-1} - \tilde{q}^{-1})/2$ and $\Gamma_+ = (\tilde{\lambda}^{-1} + \tilde{q}^{-1})/2$, and we divide the full equation Eq. (A14) by $2\tilde{\lambda}$ to find

$$\Gamma_+\mathbf{CP} + \mathbf{C} + \Gamma_-\tilde{\mathbf{P}}\mathbf{C} + \tilde{q}^{-1}\Gamma_-\tilde{\mathbf{P}}\mathbf{CP} + 2\tilde{\lambda}\tilde{q}^{-1}\Gamma_-\tilde{\mathbf{P}}\mathbf{Y} + \tilde{\lambda}\tilde{q}^{-1}\mathbf{Y} + \mathbf{\Omega}_a = 0.$$

We can now compute the projections $\mathbf{u}_i^T \mathbf{C} \mathbf{u}_j$. We multiply this equation by $\mathbf{u}_i^T$ and $\mathbf{u}_j$ respectively on the left and on the right, and we denote $c_{ij} = \mathbf{u}_i^T \mathbf{C} \mathbf{u}_j$ and $\omega_{ij} = \mathbf{u}_i^T \mathbf{\Omega}_a \mathbf{u}_j$ and $\eta_{ij} = \mathbf{u}_i^T \mathbf{Y} \mathbf{u}_j$

$$c_{ij}\left[\Gamma_+\gamma_j + 1 + \Gamma_-\frac{\gamma_i}{1+\gamma_i\tilde{q}^{-1}} + \tilde{q}^{-1}\Gamma_-\frac{\gamma_i\gamma_j}{1+\gamma_i\tilde{q}^{-1}}\right] = -\tilde{\lambda}\tilde{q}^{-1}\eta_{ij} - 2\tilde{\lambda}\tilde{q}^{-1}\Gamma_-\frac{\gamma_i}{1+\gamma_i\tilde{q}^{-1}}\eta_{ij} - \omega_{ij}$$

$$= -\tilde{\lambda}\tilde{q}^{-1}\frac{1+\gamma_i\tilde{\lambda}^{-1}}{1+\gamma_i\tilde{q}^{-1}}\eta_{ij} - \omega_{ij}.$$

The term in brackets reads is always positive and reads

$$\Gamma_+\gamma_j + 1 + \Gamma_-\frac{\gamma_i}{1+\gamma_i\tilde{q}^{-1}} + \tilde{q}^{-1}\Gamma_-\frac{\gamma_i\gamma_j}{1+\gamma_i\tilde{q}^{-1}} = \frac{\tilde{q}^{-1}\tilde{\lambda}^{-1}\gamma_i\gamma_j + (\gamma_i+\gamma_j)\Gamma_+ + 1}{1+\gamma_i\tilde{q}^{-1}},$$

leading us to

$$c_{ij} = -\frac{\tilde{\lambda}\tilde{q}^{-1}\eta_{ij}(1+\gamma_i\tilde{\lambda}^{-1}) + \omega_{ij}(1+\gamma_i\tilde{q}^{-1})}{\tilde{q}^{-1}\tilde{\lambda}^{-1}\gamma_i\gamma_j + \Gamma_+(\gamma_i+\gamma_j) + 1}.$$

Knowing the matrix elements of $\mathbf{C}$ in the basis $\mathbf{U}$, we can write $\mathbf{C}$ as a sum of outer products

$$\mathbf{C} = \sum_{i,j} c_{ij}\mathbf{u}_i\mathbf{u}_j^T,$$

such that the solution reads

$$\mathbf{C} = -\sum_{i,j}\frac{\tilde{\lambda}\tilde{q}^{-1}\eta_{ij}(1+\gamma_i\tilde{\lambda}^{-1}) + \omega_{ij}(1+\gamma_i\tilde{q}^{-1})}{\tilde{q}^{-1}\tilde{\lambda}^{-1}\gamma_i\gamma_j + \Gamma_+(\gamma_i+\gamma_j) + 1}\mathbf{u}_i\mathbf{u}_j^T. \tag{A15}$$

$\square$

In the case $\mathbf{P} = 0$ only the symmetric part can be inferred and the solution reduces to $\hat{\mathbf{\Omega}} = \Omega_s(1 - \tilde{\lambda}\tilde{q}^{-1})\mathbf{I}$. The skew symmetric part is only observable through rigid-body rotations of the distribution, which are not observable when the mean is zero. In order to work out the $\lambda \to 0$ limit, we introduce $l = \mathrm{rank}(\mathbf{P})$ which defines the ambient dimension of the inferred process. It is also useful to separate the sum in four quadrants $(i \le l, j \le l)$, $(i > l, j \le l)$, $(i \le l, j > l)$ and $(i \le l, j > l)$. By doing so, in the limit $\lambda \to 0$ we find that the minimum tends to

$$\hat{\mathbf{\Omega}} = \mathbf{\Omega} - (\mathbf{I} - \mathbf{Q})(\mathbf{\Omega}_a + rq^{-1}(\hat{\mathbf{D}} - D\mathbf{I}))(\mathbf{I} - \mathbf{Q}) - 2\sum_{\substack{j\le d \\ i\le l}}\frac{\gamma_i rq^{-1}\mu_{ij}}{2q^{-1}\gamma_i\gamma_j + \gamma_i + \gamma_j}\mathbf{u}_i\mathbf{u}_j^T, \tag{A16}$$

where $\mathbf{Q}$ is the orthogonal projector on $\mathrm{range}(\mathbf{P})$ and $\mu_{ij} = \mathbf{u}_i^T(\hat{\mathbf{D}} - D\mathbf{I})\mathbf{u}_j$. If $\mathrm{rank}(\mathbf{P}) \ge d-1$ and $\hat{\mathbf{D}} = \mathbf{D}$ we recover the true matrix $\hat{\mathbf{\Omega}} = \mathbf{\Omega}$. Assuming $\hat{\mathbf{D}} = \mathbf{D}$, we can provide an approximation to Eq. (A15) when $|\tilde{\lambda}^{-1}\gamma_i - 1| \gg 1$ and $\tilde{\lambda} \ll q$. To derive it we need to separate the sum in four quadrants $(\gamma_i \ll \tilde{\lambda}, \gamma_j \ll \tilde{\lambda})$, $(\gamma_i \ll \tilde{\lambda}, \gamma_j \gg \tilde{\lambda})$, $(\gamma_i \gg \tilde{\lambda}, \gamma_j \ll \tilde{\lambda})$, $(\gamma_i \gg \tilde{\lambda}, \gamma_j \gg \tilde{\lambda})$. In the first quadrant the denominator reduces to 1 and the numerator to ω_{ij}. The sum then reads

$$\sum_{\substack{\gamma_i\ll\tilde{\lambda} \\ \gamma_j\ll\tilde{\lambda}}}\frac{\tilde{\lambda}\tilde{q}^{-1}\eta_{ij}(1+\gamma_i\tilde{\lambda}^{-1}) + \omega_{ij}(1+\gamma_i\tilde{q}^{-1})}{\tilde{q}^{-1}\tilde{\lambda}^{-1}\gamma_i\gamma_j + \Gamma_+(\gamma_i+\gamma_j) + 1}\mathbf{u}_i\mathbf{u}_j^T = \sum_{\substack{\gamma_i\ll\tilde{\lambda} \\ \gamma_j\ll\tilde{\lambda}}}\omega_{ij}\mathbf{u}_i\mathbf{u}_j^T = \mathbf{Q}_{\tilde{\lambda}}\mathbf{\Omega}_a\mathbf{Q}_\lambda,$$

where $\mathbf{Q}_{\tilde{\lambda}}$ is the orthogonal projector on this first quadrant. In the second quadrant, the denominator will, at worst be of order $\gamma_j\tilde{\lambda}^{-1} \gg 1$, and the numerator of order 1, such that the sum vanishes. In the third quadrant the denominator will be, at worst, of order $\gamma_i\tilde{\lambda}^{-1} \gg 1$, and the numerator reduces to $\tilde{\lambda}q^{-1}\gamma_i\tilde{\lambda}^{-1}\eta_{ij} + \omega_{ij}$, such that the sum vanishes since $\tilde{\lambda}q^{-1} \ll 1$. In the last quadrant, the sum vanishes for the same reasons, such we have, under the aforementioned conditions on $\tilde{\lambda}$ and the γ_i's

$$\hat{\mathbf{\Omega}} \approx \mathbf{\Omega} - \mathbf{Q}_{\tilde{\lambda}}\mathbf{\Omega}_a\mathbf{Q}_{\tilde{\lambda}}.$$

b. Solution in the absence of regularization. When $\lambda = 0$, any minimum of the loss function is attained at

$$\hat{\boldsymbol{\Omega}} = \boldsymbol{\Omega} - rq^{-1}(\mathbf{I} - \mathbf{Q})(\hat{\mathbf{D}} - D\mathbf{I})(\mathbf{I} - \mathbf{Q}) - 2\sum_{\substack{j > l \\ i \leq l}} \frac{\gamma_i r q^{-1} \mu_{ij}}{2q^{-1}\gamma_i\gamma_j + \gamma_i + \gamma_j} \mathbf{u}_i \mathbf{u}_j^T + \mathbf{K},$$

with $\mathbf{K}$ any skew-symmetric matrix such that $\mathbf{KP} = 0$ and $\mu_{ij} = \mathbf{u}_i^T(\hat{\mathbf{D}} - D\mathbf{I})\mathbf{u}_j$. This minimum is unique if and only if $\text{rank}(\mathbf{P}) \geq d - 1$, in which case it is obtained as $\lambda \to 0$ in Eq. (A16).

Proof. In the case $\lambda = 0$ the equation for c_{ij} can be obtained for $(i \leq l, j > l)$, $(i \leq l, j \leq l)$ or $(i > l, j \leq l)$ by taking $\lambda \to 0$

$$c_{ij}\left[\gamma_j + \frac{\gamma_i}{1 + \gamma_i q^{-1}} + \frac{q^{-1}\gamma_i\gamma_j}{1 + \gamma_i q^{-1}}\right] = -\frac{2\gamma_i r q^{-1}\mu_{ij}}{1 + \gamma_i q^{-1}}.$$

On the other hand, c_{ij} is undetermined for $i, j > l$. However, it must also satisfy Eq. (A11), such that for $i, j > l$ we have

$$c_{ij} + c_{ji} = -2rq^{-1}\mu_{ij}.$$

This only constrains the symmetric part of $\mathbf{C}$ on the orthogonal complement of range($\mathbf{P}$), which leaves us with the solution

$$\hat{\boldsymbol{\Omega}} = \boldsymbol{\Omega} - rq^{-1}(\mathbf{I} - \mathbf{Q})(\hat{\mathbf{D}} - D\mathbf{I})(\mathbf{I} - \mathbf{Q}) - 2\sum_{\substack{j \leq d \\ i \leq l}} \frac{\gamma_i r q^{-1} \mu_{ij}}{2q^{-1}\gamma_i\gamma_j + \gamma_i + \gamma_j} \mathbf{u}_i \mathbf{u}_j^T + \mathbf{K},$$

where $\mathbf{K}$ denotes any skew-symmetric matrix such that $\mathbf{KP} = 0$. We then see that if $\text{rank}(\mathbf{P}) \geq d - 1$ then $\mathbf{K} = 0$ is the only option such that the solution is unique and corresponds to Eq. (A16). $\square$

4. Variance in the isotropic case

We are interested in quantifying the finite sample size error incurred on the estimation of the interaction matrix $\hat{\boldsymbol{\Omega}}$. For this we can derive a finite sample size loss using the central limit theorem, which holds for large enough sample size and small enough time step.

a. Central limit theorem. Let $\mathbf{x}_1, ..., \mathbf{x}_n$ be independent samples drawn from a probability law $\mathbb{P}$. We will denote the sample covariance and sample mean of this law as

$$\mathbf{m}_n = \frac{1}{n}\sum_{i=1}^{n}\mathbf{x}_i \text{ and } \boldsymbol{\Sigma}_n = \frac{1}{n-1}\sum_{i=1}^{n}(\mathbf{x}_i - \mathbf{m}_n)(\mathbf{x}_i - \mathbf{m}_n)^T.$$

Then, if $\mathbb{P} = \mathcal{N}(\mathbf{m}, \boldsymbol{\Sigma})$, we have the following asymptotic results (see [48] Lemma 4.2.)

$$\sqrt{n}(\mathbf{m}_n - \mathbf{m}) \xrightarrow[n\to\infty]{d} \boldsymbol{\Sigma}^{1/2}\mathbf{h} \text{ and } \sqrt{n}(\boldsymbol{\Sigma}_n - \boldsymbol{\Sigma}) \xrightarrow[n\to\infty]{d} \boldsymbol{\Sigma}^{1/2}\mathbf{H}\boldsymbol{\Sigma}^{1/2},$$

where $\mathbf{h}$ and $\mathbf{H}$ are independent random variables such that $\mathbf{h} \sim \mathcal{N}(0, \mathbf{I})$ and $\mathbf{H}$ is drawn from the Gaussian Orthogonal Ensemble (GOE), ie $\mathbf{H}$ is a real random symmetric matrix with entries satisfying

$$H_{ij} = \begin{cases} \mathcal{N}(0,1), & \text{if } i > j \\ \mathcal{N}(0,2), & \text{if } i = j \end{cases}.$$

b. Delta method for the Wasserstein distance. Let's assume that we have the following asymptotic expansion $\boldsymbol{\Sigma}_n \xrightarrow{d} \boldsymbol{\Sigma} + \mathbf{G}/\sqrt{n}$, $\hat{\boldsymbol{\Sigma}}_n = \hat{\boldsymbol{\Sigma}} + \hat{\mathbf{G}}/\sqrt{n}$, $\mathbf{m}_n \xrightarrow{d} \mathbf{m} + \mathbf{g}/\sqrt{n}$ and $\boldsymbol{\Sigma}, \hat{\mathbf{m}}_n \xrightarrow{d} \hat{\mathbf{m}} + \hat{\mathbf{g}}/\sqrt{n}$ where $\mathbf{g}, \hat{\mathbf{g}}, \mathbf{G}, \mathbf{G}$ are random variables. We also assume that $\hat{\boldsymbol{\Sigma}}$ and $\boldsymbol{\Sigma}$ commute. Combining the results of Lemma 2.3, Remark 2.6 and Theorem 4.1 of [48], the delta method provides us with the following asymptotic result

$$\sqrt{\frac{n}{2}}\left(\mathcal{W}_2^2\left(\mathcal{N}(\hat{\mathbf{m}}_n, \hat{\boldsymbol{\Sigma}}_n), \mathcal{N}(\mathbf{m}_n, \boldsymbol{\Sigma}_n)\right) - \mathcal{W}_2^2\left(\mathcal{N}(\hat{\mathbf{m}}, \hat{\boldsymbol{\Sigma}}), \mathcal{N}(\mathbf{m}, \boldsymbol{\Sigma})\right)\right) \xrightarrow[n\to+\infty]{d} \xi,$$

where $\xrightarrow{d}$ means convergence in distribution, and ξ is a random variable satisfying

$$\xi = \sqrt{2}(\mathbf{m} - \hat{\mathbf{m}})^T \mathbf{g} + \sqrt{2}(\hat{\mathbf{m}} - \mathbf{m})^T \hat{\mathbf{g}} + \frac{1}{\sqrt{2}} \text{tr}(\boldsymbol{\Sigma}^{-1/2}(\boldsymbol{\Sigma}^{1/2} - \hat{\boldsymbol{\Sigma}}^{1/2})\mathbf{G}) + \frac{1}{\sqrt{2}} \text{tr}(\hat{\boldsymbol{\Sigma}}^{-1/2}(\hat{\boldsymbol{\Sigma}}^{1/2} - \boldsymbol{\Sigma}^{1/2})\hat{\mathbf{G}}). \quad \text{(A17)}$$

When $\mathbf{m} = \hat{\mathbf{m}}$ and $\boldsymbol{\Sigma} = \hat{\boldsymbol{\Sigma}}$ the Fréchet derivative of the loss vanishes [48], and the second order delta method has to be applied.

c. *Finite sample size loss* With finitely many samples $\hat{p}_{t_i}$ and p_{t_i} are discrete distribution. In particular, the estimation of the Wasserstein loss from this finite sample size distributions will suffer from the curse of dimensionality [46]. As we are working with Gaussian distributions we can avoid this issue by replacing the finite sample size Wasserstein distance by its Gaussian estimator [48]. The Gaussian estimator of the Wasserstein distance is defined as follows

$$\mathcal{GW}_2^2(\hat{\nu}_{t_i}, \nu_{t_i}) = \mathcal{W}_2^2\left(\mathcal{N}(\hat{\mathbf{m}}_{n,t_i}, \hat{\boldsymbol{\Sigma}}_{n,t_i}), \mathcal{N}(\mathbf{m}_{n,t_i}, \boldsymbol{\Sigma}_{n,t_i})\right), \quad \text{(A18)}$$

where $\hat{\mathbf{m}}_{n,\Delta t}, \hat{\boldsymbol{\Sigma}}_{n,t_i}$ and $\mathbf{m}_{n,t_i}, \boldsymbol{\Sigma}_{n,t_i}$ are the sample mean and sample covariance of the inferred and true processes, respectively. Using the delta method Eq. (A18), the finite sample size loss reads

$$\mathcal{L}_{\Delta t, K_{\Delta t}} = \sum_{i=0}^{K_{\Delta t}-2} \left[\mathcal{W}_2^2(\hat{p}_{t_i+\Delta t}, p_{t_i+\Delta t}) + \sqrt{\frac{2}{n}} \xi\left(\hat{\mathbf{m}}_{t_i+\Delta t}, \hat{\boldsymbol{\Sigma}}_{t_i+\Delta t}, \mathbf{m}_{t_i+\Delta t}, \boldsymbol{\Sigma}_{t_i+\Delta t}\right) \right] + \lambda K \Delta t^2 \|\hat{\boldsymbol{\Omega}}\|_F^2 + o\left(\frac{1}{\sqrt{n}}\right).$$

Similarly to the $n \to \infty$ case, we consider the term $t_0 = 0$ in the above sum. In order to perform a small Δt expansion of the finite sample size term ξ, we need to explicit the random terms $\hat{\mathbf{G}}, \mathbf{G}, \hat{\mathbf{g}}, \mathbf{g}$ in Eq. (A17). How these terms depend on $\hat{\mathbf{m}}_{\Delta t}, \hat{\boldsymbol{\Sigma}}_{\Delta t}, \mathbf{m}_{\Delta t}$ and $\boldsymbol{\Sigma}_{\Delta t}$, and whether they are correlated with one another depends on how the true process and the inferred are generated. Samples from the true process are independent from one another, but samples of the inferred process are generated by pushing the true samples using the probability flow ODE. The estimated mean and covariance of the inferred process then read

$$\hat{\mathbf{m}}_{n,\Delta t} = \frac{1}{n} \sum_k \hat{\mathbf{x}}_{k,\Delta t} = \left(\mathbf{I} + \Delta t \hat{\boldsymbol{\Omega}}\right) \mathbf{m}_{n,0} + \hat{\mathbf{D}} \Sigma_0^{-1}(\mathbf{m}_{n,0} - \mathbf{m}_0),$$

$$\hat{\boldsymbol{\Sigma}}_{n,\Delta t} = \frac{1}{n} \sum_k (\hat{\mathbf{x}}_{k,\Delta t} - \hat{\mathbf{m}}_{n,\Delta t})(\hat{\mathbf{x}}_{k,\Delta t} - \hat{\mathbf{m}}_{n,\Delta t})^T = (\mathbf{I} + \Delta t(\hat{\boldsymbol{\Omega}} + \hat{\mathbf{D}} \Sigma_0^{-1}))\boldsymbol{\Sigma}_{0,n}(\mathbf{I} + \Delta t(\hat{\boldsymbol{\Omega}} + \hat{\mathbf{D}} \Sigma_0^{-1}))^T.$$

We can now apply the central limit theorem for the sample mean and sample covariance of the true process

$$\boldsymbol{\Sigma}_{n,0} = \boldsymbol{\Sigma}_0 + \frac{1}{\sqrt{n}} \boldsymbol{\Sigma}_0^{1/2} \mathbf{H}_0 \boldsymbol{\Sigma}_0^{1/2}, \ \mathbf{m}_{n,0} = \mathbf{m}_0 + \frac{1}{\sqrt{n}} \boldsymbol{\Sigma}_0^{1/2} \mathbf{h}_0,$$

$$\boldsymbol{\Sigma}_{n,\Delta t} = \boldsymbol{\Sigma}_{\Delta t} + \frac{1}{\sqrt{n}} \boldsymbol{\Sigma}_{\Delta t}^{1/2} \mathbf{H}_{\Delta t} \boldsymbol{\Sigma}_{\Delta t}^{1/2}, \ \mathbf{m}_{n,\Delta t} = \mathbf{m}_{\Delta t} + \frac{1}{\sqrt{n}} \boldsymbol{\Sigma}_{\Delta t}^{1/2} \mathbf{h}_{\Delta t},$$

and

$$\mathbf{g}_{\Delta t} = \Sigma_{\Delta t}^{1/2} \mathbf{h}_{\Delta t}, \ \mathbf{G}_{\Delta t} = \boldsymbol{\Sigma}_{\Delta t} \mathbf{H}_{\Delta t}.$$

Making use of the fact that the covariance of the true process is isotropic we have for the inferred process

$$\hat{\mathbf{m}}_{n,\Delta t} = \hat{\mathbf{m}}_{\Delta t} + \frac{1}{\sqrt{n}} \hat{\mathbf{g}}_{\Delta t}, \ \hat{\boldsymbol{\Sigma}}_{n,\Delta t} = \hat{\boldsymbol{\Sigma}}_{\Delta t} + \frac{1}{\sqrt{n}} \hat{\mathbf{G}}_{\Delta t},$$

with, at first order in Δt

$$\hat{\boldsymbol{\Sigma}}_{\Delta t} = \boldsymbol{\Sigma}_0 + \Delta t((\hat{\boldsymbol{\Omega}} + \hat{\boldsymbol{\Omega}}^T)\Sigma_0 + 2\hat{\mathbf{D}}), \ \hat{\mathbf{G}}_{\Delta t} = \Sigma_0 \mathbf{H}_0 + \Delta t(\hat{\boldsymbol{\Omega}} + \hat{\mathbf{D}} \Sigma_0^{-1})\Sigma_0 \mathbf{H}_0 + \Sigma_0 \mathbf{H}_0 (\hat{\boldsymbol{\Omega}} + \hat{\mathbf{D}} \Sigma_0^{-1})^T,$$

$$\hat{\mathbf{m}}_{\Delta t} = \left(\mathbf{I} + \Delta t \hat{\boldsymbol{\Omega}}\right) \mathbf{m}_0, \ \hat{\mathbf{g}}_{\Delta t} = \Sigma_0^{1/2} \mathbf{h}_0 + \Delta t \Sigma_0^{1/2}(\hat{\boldsymbol{\Omega}} + \hat{\mathbf{D}} \Sigma_0^{-1}) \mathbf{h}_0.$$

We can now perform the small Δt expansion of ξ. We keep terms up to order Δt, and the noise term ξ reads

$$\xi\left(\hat{\mathbf{m}}_{\Delta t}, \hat{\boldsymbol{\Sigma}}_{\Delta t}, \mathbf{m}_{\Delta t}, \boldsymbol{\Sigma}_{\Delta t}\right) = \sqrt{2} \Delta t \Sigma_0^{1/2} \mathbf{m}_0^T (\hat{\boldsymbol{\Omega}} - \boldsymbol{\Omega})^T (\mathbf{h}_0 - \mathbf{h}_{\Delta t}) + \frac{\Sigma_0 \Delta t}{2\sqrt{2}} \text{tr}\left(\left(\hat{\boldsymbol{\Omega}} + \hat{\boldsymbol{\Omega}}^T - 2\Omega_s\right)(\mathbf{H}_0 - \mathbf{H}_{\Delta t})\right).$$

We note here that the noise term is of order Δt while the infinite sample size loss is of order Δt^2. This happens because the noise terms $\hat{\mathbf{G}}_{\Delta t}, \mathbf{G}_{\Delta t}$ and $\hat{\mathbf{g}}_{\Delta t}, \mathbf{g}_{\Delta t}$ are different at order Δt. If the true and inferred process were pushed from the same distribution at time $t_0 = 0$ and then compared at time Δt, the sources of randomness would match at order Δt such that the noise term and the continuous-time loss would be of both of order Δt^2. The fact that they are not of the same order here limits the inference at small Δt, since the noise term will dominate in this regime. This will in fact reflect in the estimation of the variance that will diverge when $\Delta t \to 0$. The finite sample size loss reads

$$\mathcal{L}_n = \mathcal{L} + \frac{\sqrt{2}}{\sqrt{n}\Delta t}\left(\sqrt{2}\mathrm{tr}\left[(\hat{\mathbf{\Omega}} - \mathbf{\Omega})^T \int_0^T \sigma_t(\mathbf{h}_t - \mathbf{h}_{t+\Delta t})\mathbf{m}_t^T\, dt \right] + \mathrm{tr}\frac{1}{2\sqrt{2}}\left[(\hat{\mathbf{\Omega}} + \hat{\mathbf{\Omega}}^T - 2\Omega_s\mathbf{I})\int_0^T \sigma_t^2(\mathbf{H}_t - \mathbf{H}_{t+\Delta t})dt \right] \right).$$

The noise terms are telescoping series up to order Δt^2 terms, which allows us to simplify further the loss

$$\mathcal{L}_n = \mathcal{L} + \frac{\sqrt{2}}{\sqrt{n}\Delta t}\left(\sqrt{2}\mathrm{tr}\left[(\hat{\mathbf{\Omega}} - \mathbf{\Omega})^T \mathbf{Y} \right] + \mathrm{tr}\frac{1}{2\sqrt{2}}\left[(\hat{\mathbf{\Omega}} + \hat{\mathbf{\Omega}}^T - 2\Omega_s\mathbf{I})\mathbf{W} \right] \right),$$

where we have introduced

$$\mathbf{Y} = \sigma_0\mathbf{h}_0\mathbf{m}_0^T - \sigma_T\mathbf{h}_T\mathbf{m}_T^T \text{ and } \mathbf{W} = \sigma_0^2\mathbf{H}_0 - \sigma_T^2\mathbf{H}_T.$$

    d.   First order finite sample size correction $\hat{\mathbf{\Omega}}_{\cdot 1}$ The first order optimality condition for the finite sample loss reads

$$\frac{\partial \mathcal{L}}{\partial \mathbf{\Omega}} + \frac{\sqrt{2}}{\sqrt{n}\Delta t}\left(\sqrt{2}\mathbf{Y} + \frac{1}{\sqrt{2}}\mathbf{W} \right) = 0,$$
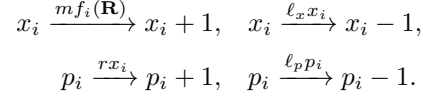
such that the first correction $\hat{\mathbf{\Omega}}_1$ to the interaction matrix due to finite sample size reads

$$\hat{\mathbf{\Omega}}_1 = -\sum_{i,j} \frac{\tilde{\lambda}\tilde{q}^{-1}\eta_{ij}(1 + \gamma_i\tilde{\lambda}^{-1}) + \omega_{ij}(1 + \gamma_i\tilde{q}^{-1})}{\tilde{q}^{-1}\tilde{\lambda}^{-1}\gamma_i\gamma_j + \Gamma_+(\gamma_i + \gamma_j) + 1}\mathbf{u}_i\mathbf{u}_j^T,$$

with $\eta_{ij} = \mathbf{u}_i^T\mathbf{Z}_s\mathbf{u}_j$ and $\omega_{ij} = \mathbf{u}_i^T\mathbf{Z}_a\mathbf{u}_j$ where $\mathbf{Z}_a$ and $\mathbf{Z}_s$ respectively the skew-symmetric and symmetric part of $\mathbf{Z} = (\mathbf{Y} + \mathbf{W}/2)/(\tilde{\lambda}n^{-1/2}\Delta t)$. From this first correction, the first contribution to the variance is readily computed as $\mathbb{E}\|\hat{\mathbf{\Omega}}_1\|_F^2$.

Appendix B: Generating gene expression data

a. BooldODE formalism. The Chemical Master Equation (CME) provides a framework for modeling stochastic gene transcription dynamics [60]. Gillespie's stochastic simulation algorithm (SSA) [86], [87] allows for the computation of reaction trajectories governed by the CME. For gene transcription and translation, the key reactions are:

$$x_i \xrightarrow{m f_i(\mathbf{R})} x_i + 1, \quad x_i \xrightarrow{\ell_x x_i} x_i - 1,$$

$$p_i \xrightarrow{r x_i} p_i + 1, \quad p_i \xrightarrow{\ell_p p_i} p_i - 1.$$

Here, x_i represents mRNA molecules, and p_i denotes protein molecules. The propensities for these reactions incorporate the regulatory interactions controlling the expression of gene (or node) i. These interactions can be expressed as:

$$\Pr(S) = \frac{\prod_{p \in S} \left(\frac{p}{k}\right)^n}{1 + \sum_{S \in 2^{R_i} - 1} \prod_{p \in S} \left(\frac{p}{k}\right)^n},$$

and the regulation function is defined as:

$$f(R_i) = \sum_{S \in 2^{R_i}} \alpha_S \Pr(S).$$

In this formulation, the product in the numerator accounts for all bound regulators in a given configuration S, while the sum in the denominator includes all possible configurations in the powerset of regulators R_i, excluding the empty set. The parameters are defined as $m = 20$, $\ell_x = 5$, $r = 1$, $\ell_p = 1$, $k = 10$, and $n = 10$, following [69]. To simplify the system and reduce the number of variables, we assume that protein dynamics equilibrate faster than mRNA dynamics. Under this approximation, the protein abundance can be expressed in terms of mRNA levels, i.e., $\bar{p}_i = \left(\frac{r}{\ell_p}\right) x_i$. This assumption, while commonly used, may or may not hold depending on the biological system in question. In some cases, the reverse limit—where mRNA equilibrates faster than protein (known as the quasi-steady-state approximation, QSSA)—is equally valid and more widely adopted.

b. mCAD model. The Boolean rules associated with the mCAD network are adapted from [88],

$$P \leftarrow \neg C \wedge \neg E \wedge S; \quad S \leftarrow F \wedge \neg E; \quad F \leftarrow F \wedge S \wedge \neg E; \quad E \leftarrow \neg F \wedge \neg P \wedge \neg S \wedge C; \quad C \leftarrow \neg S \wedge \neg F.$$

For instance, the propensity function f_P for $k = n = 1$, is

$$f_p(R) = \left(\frac{[S]}{1 + [C] + [E] + [S] + [C][E] + [E][S] + [C][S] + [C][S][E]} \right).$$

c. HSC model. The Boolean rules associated with the HSC model are taken from [71],

$$G1 \leftarrow (G1 \vee G2 \vee Fli) \wedge \neg P; \quad G2 \leftarrow G2 \wedge \neg(G1 \wedge Fg) \wedge \neg P; \quad Fg \leftarrow G1; \quad E \leftarrow G1 \wedge \neg Fli;$$

$$Fli \leftarrow G1 \wedge \neg E; \quad S \leftarrow G1 \wedge \neg P; \quad Ceb \leftarrow Ceb \wedge \neg(G1 \wedge Fg \wedge S); \quad P \leftarrow (Ceb \vee P) \wedge \neg(G1 \vee G2);$$

$$cJ \leftarrow (P \wedge \neg G); \quad Eg \leftarrow (P \wedge cJ) \wedge \neg G; \quad G \leftarrow (Ceb \wedge \neg Eg).$$

Appendix C: Score validation

After training a neural network to approximate the score function $s_\theta(\mathbf{x}) \approx \nabla_\mathbf{x} \log p_{\text{data}}(\mathbf{x})$, Langevin dynamics can be used to sample from the target distribution $p_{\text{data}}(\mathbf{x})$. Starting with a fixed step size $\epsilon > 0$ and an initial value $\tilde{\mathbf{x}}_0 \sim \pi(\mathbf{x})$, where π is a prior distribution, the Langevin method iteratively updates the samples using the equation:

$$\tilde{\mathbf{x}}_t = \tilde{\mathbf{x}}_{t-1} + \frac{\epsilon}{2}\nabla_\mathbf{x} \log p(\tilde{\mathbf{x}}_{t-1}) + \sqrt{\epsilon}\mathbf{z}_t,$$

where $\mathbf{z}_t \sim \mathcal{N}(0, I)$. Under certain conditions, as $\epsilon \to 0$ and $T \to \infty$, the distribution of $\tilde{\mathbf{x}}_T$ converges to $p(\mathbf{x})$, resulting in exact samples from $p(\mathbf{x})$ [89]. For finite ϵ and T, a Metropolis-Hastings update is often used to correct the approximation, though this correction is typically negligible for small ϵ and large T [90]. This sampling approach relies only on the score function $\nabla_\mathbf{x} \log p(\mathbf{x})$. We validate the score model by running Langevin dynamics to generate samples and evaluate how accurately they match the cross-sectional data.

	Dimension (d)	# hidden layers	# nodes	# snapshots (K)/ Δt	# samples (n)
Ornstein-Ulhenbeck	10	3	50	10/0.05	8000
Cyclic SRN	30	4	100	10/0.04	10000
mCAD	5	4	50	10/0.04	6000
HSC	11	6	100	8/0.04	5000

TABLE I. Hyper-parameters of the different network architectures used for training the score network $\mathbf{s}_\phi : \mathbb{R}^{d+1} \to \mathbb{R}^d$.
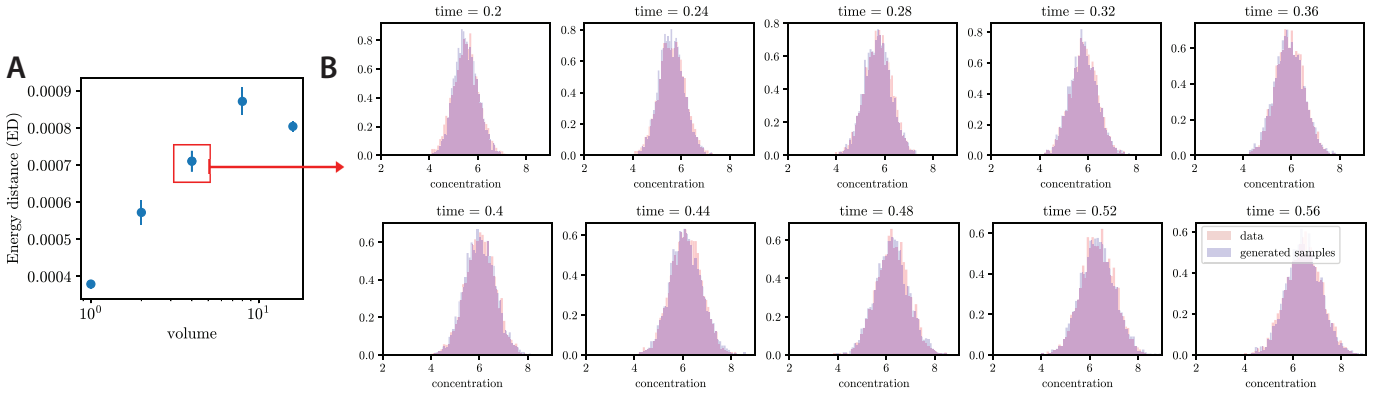
FIG. S1. **Score validation for linear cyclic network** ($d = 30$): **A.** Energy distance between the generated samples from Langevin dynamics and the marginal data for different reaction volumes (V). **B.** Histograms of concentration values over time for both real data (red) and generated samples (blue) are compared for specific volume ($V = 4$) is highlighted in panel **A.**. The times range from 0.2 to 0.56, showing the evolution of the distribution of concentration values.
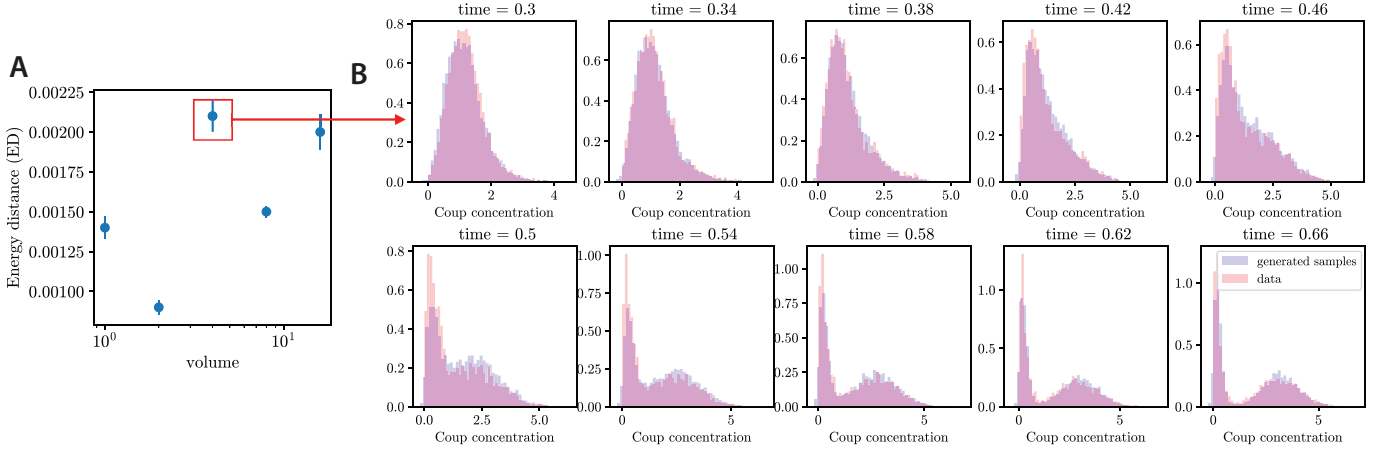

FIG. S2. **Score validation for mCAD network** ($d = 5$): **A.** Energy distance between the generated samples from Langevin dynamics and the marginal data for different reaction volumes (V). **B.** Histograms showing the time evolution of mRNA concentration values for the *Coup* gene, comparing real data (red) and generated samples (blue), are shown for a specific volume ($V = 4$), as highlighted in panel **A.**.
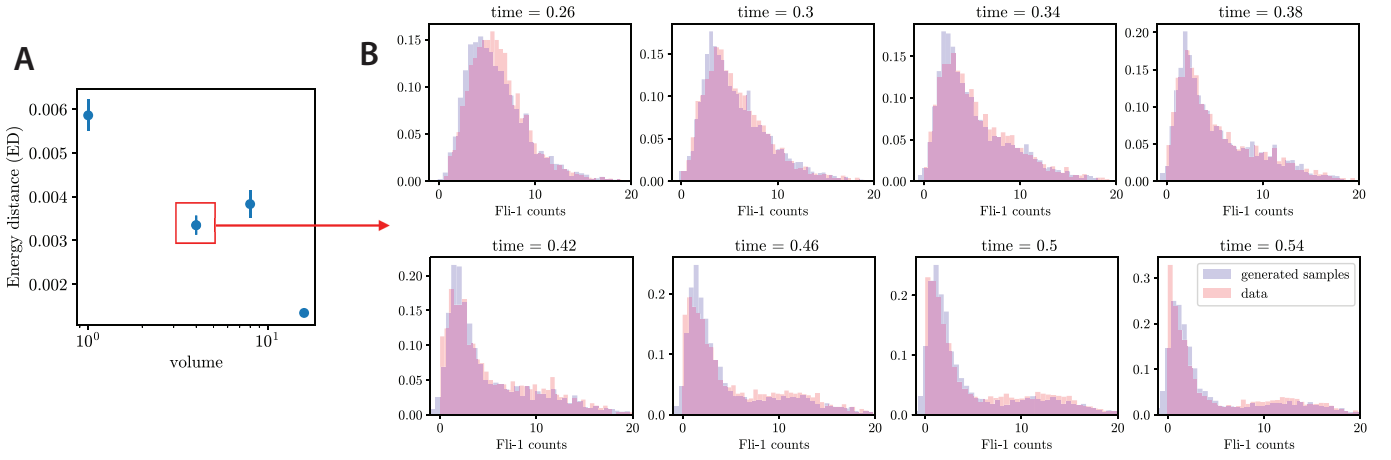
FIG. S3. **Score validation for HSC network** ($d = 11$): **A.** Energy distance between the generated samples from Langevin dynamics and the marginal data for different reaction volumes (V). **B. B.** Histograms showing the time evolution of mRNA concentration values for the *Fli-1* gene over evolving, comparing real data (red) and generated samples (blue), are shown for a specific volume ($V = 4$), as highlighted in panel **A.**
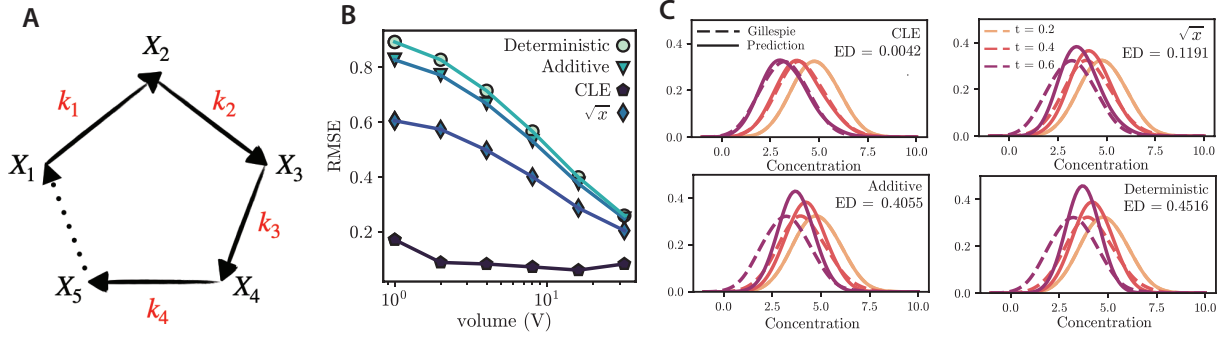

FIG. S4. **Parameter estimation in linear cyclic stochastic reaction network: A.** Schematic of the linear cyclic network. **B.** The RMSE $\|\hat{\mathbf{k}} - \mathbf{k}\|_2^2 / \|\mathbf{k}\|_2^2$ of the inferred rate constants shown for different compartment volumes V. **C.** Comparison of empirical marginals generated from the inferred diffusion process under various noise forms (inset) with marginals generated from Gillespie's simulation with $V = 4$.
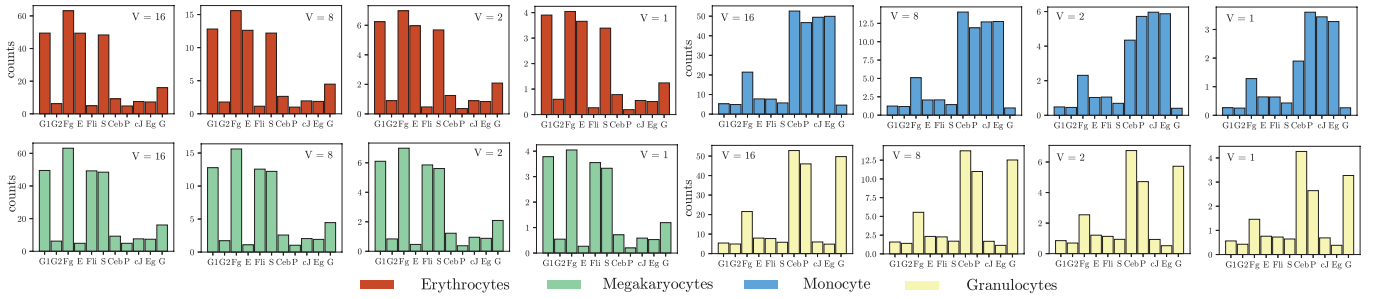

FIG. S5. Average molecular counts as a function of the reaction volume (V) in each cell type represented by different colors. The y-axis represents the average molecular counts, highlighting the effect of varying reaction volumes on the observed counts.